Report no. 95/10

Preconditioning on Stretched Meshes

Niles A. Pierce Michael B. Giles
Oxford University Computing Laboratory
Numerical Analysis Group

High aspect ratio cells in a computational mesh compound the inherent stiffness in the Euler and Navier–Stokes equations which arises from a disparity in the propagative speeds of convective and acoustic modes. A mesh-aligned preconditioning strategy is examined which is intended to improve multigrid performance in two ways: a) enhancing propagation of disturbances by shaping wave front envelopes to match cell aspect ratios, b) clustering high frequency components of the spatial Fourier footprint away from the origin for effective damping by an optimized Runge-Kutta time stepping scheme. In contrast to previous approaches, the method is robust when used in conjunction with high resolution schemes on fine meshes and with multigrid. Results are provided for a number of standard airfoil test cases.

Key words and phrases: CFD, compressible flow, preconditioning, stretched meshes

This work was funded by the Rhodes Trust.

Oxford University Computing Laboratory
Numerical Analysis Group
Wolfson Building
Parks Road
Oxford, England OX1 3QD
E-mail: Niles.Pierce@comlab.oxford.ac.uk

June, 1995

Contents

1 Introduction **3**

2 Approach **3**
2.1 Scalar Preconditioner 4
2.2 Diagonal Preconditioner 5
2.3 Block-Jacobi Preconditioner 7

3 Analysis **8**
3.1 Fourier Footprints and Wave Front Envelopes 8
3.2 Analytic Asymptotic Results 11

4 Results **12**
4.1 Euler 14
4.2 Laminar Navier–Stokes 15

5 Conclusions **17**

1 Introduction

Explicit Euler and Navier–Stokes solvers based on multigrid remain popular due to ease of programming and suitability for parallelization despite the fact that convergence is significantly hampered by the use of a scalar time step limit which is appropriate only for the fastest propagating mode. Considering this problem for the Euler equations, van Leer suggested using a matrix preconditioner to approximate characteristic time stepping with the aim of achieving a unit condition number [19, 20]. This strategy leads to a stream-aligned implementation which requires a modification of the numerical dissipation, is fragile near stagnation points and does not take into account the additional stiffness arising from large cell aspect ratios [11].

Motivated by the breakdown of multigrid convergence in highly stretched boundary layer cells, Allmaras proposed the use of an implicit ADI preconditioner for full coarsening multigrid and preconditioners based on point-implicit block-Jacobi and semi-implicit line-Jacobi for the more expensive semi-coarsening multigrid algorithm of Mulder [1, 2, 13, 14]. The approach is aimed at clustering the eigenvalues of error modes for which multigrid is ineffective away from the origin so that they can be rapidly damped by a multi-stage time stepping scheme. Allmaras has demonstrated the effectiveness of this approach in improving convergence by relaxing a randomly perturbed initial state back to uniform flow on a Cartesian mesh for a wide variety of flow and mesh parameters [1, 2].

In the stretched boundary layer cells of a viscous mesh, the explicit scalar time step is limited by the transverse acoustic mode $\Delta t = O(\frac{\Delta y}{c})$, which is typically several orders of magnitude more restrictive than necessary for the streamwise and transverse convective modes, for which a more appropriate constraint is $\Delta t = O(\frac{\Delta x}{u}) = O(\frac{\Delta y}{v})$. This difference can be substantial even for Euler computations. A successful preconditioner should therefore modify the shape of the wave front envelopes so that convective and acoustic disturbances originating at the cell center both reach the cell boundary in approximately the same number of time steps.

The present work examines preconditioners based on both characteristic time stepping and block-Jacobi viewpoints in terms of wave front envelope shaping and eigenvalue clustering. Analytic results for preconditioned eigenvalue clustering are obtained for six important asymptotic limits of flow and cell variables, including two cases for the full Navier–Stokes equations. Emphasis is placed on demonstrating viability for practical aerodynamic computations.

2 Approach

A preconditioned semi-discrete finite volume scheme takes the form

$$\frac{dW_{j,k}}{dt} + PR(W) = 0, \tag{2.1}$$

where $R(W)$ is the residual vector of the spatial discretization and P is a local preconditioner designed to reduce stiffness arising from variation in the flow and mesh parameters. This work examines two matrix alternatives to the standard scalar preconditioner in common use. The first is a diagonal preconditioner that approximates characteristic time stepping by operating on a transformed system in which the modes

are only loosely coupled. The second is a block-Jacobi preconditioner based on the specific structure of the residual vector.

Analysis is performed on the linearized 2D Navier–Stokes equations in Cartesian coordinates

$$\frac{\partial W}{\partial t} + A\frac{\partial W}{\partial x} + B\frac{\partial W}{\partial y} = C\frac{\partial^2 W}{\partial x^2} + D\frac{\partial^2 W}{\partial y^2} + E\frac{\partial^2 W}{\partial x \partial y}, \tag{2.2}$$

from which the Euler equations may be obtained by eliminating the viscous terms on the right hand side. A Cartesian mesh is assumed to simplify notation, but the theory extends naturally to a (ξ, η) mesh-aligned coordinate system for real applications.

2.1 Scalar Preconditioner

The explicit stability limit for a scalar time step is based on the spectral radii of the flux Jacobians in (2.2),

$$\rho(A) = |u| + c, \quad \rho(B) = |v| + c, \quad \rho(C) = \rho(D) = \frac{\gamma\nu}{Pr}, \quad \rho(E) = \frac{\nu}{3}\,, \tag{2.3}$$

where u and v are the Cartesian velocity components, c is the speed of sound, γ is the ratio of specific heats, ν is the kinematic viscosity and Pr is the Prandtl number.

A conservative time step estimate for the Navier–Stokes equations is based on the purely hyperbolic and parabolic time steps [12],

$$\Delta t_{NS}^{-1} = \Delta t_H^{-1} + \Delta t_P^{-1}, \tag{2.4}$$

where the hyperbolic time step is given by

$$\Delta t_H^{-1} = \frac{1}{\mathrm{CFL_H}} \left(\frac{\rho(A)}{\Delta x} + \frac{\rho(B)}{\Delta y} \right) \tag{2.5}$$

and the parabolic time step is

$$\Delta t_P^{-1} = \frac{1}{\mathrm{CFL_P}} \left(\frac{4\rho(C)}{\Delta x^2} + \frac{4\rho(D)}{\Delta y^2} + \frac{\rho(E)}{\Delta x \Delta y} \right). \tag{2.6}$$

The factor of 4 in the parabolic time step arises from considering the worst-case scenario of a checker-board mode, $W_{j,k} = \widehat{W}(t)e^{i(\pi j + \pi k)}$, for which the coefficients of the 2nd difference stencil reinforce each other in both directions. The hyperbolic and parabolic CFL numbers, $\mathrm{CFL_H}$ and $\mathrm{CFL_P}$, reflect the extent of the multi-stage time stepping scheme stability region along the imaginary and negative real axes, respectively. On a real computational mesh in which Δx and Δy vary, this time step limit defines a suitable scalar preconditioner for the Navier–Stokes equations, $P_{S_{NS}}^{-1} = \Delta t_{NS}^{-1}$, that reduces stiffness resulting from variation in spectral radius and minimum cell dimension throughout the mesh.

For the Euler equations, the corresponding scalar preconditioner is defined by the purely hyperbolic time step, $P_{S_E}^{-1} = \Delta t_H^{-1}$, assuming that the numerical dissipation introduced to prevent decoupling is sufficiently small so as not to limit the stability. The implications of this assumption for the scaling of the numerical dissipation will be examined more thoroughly in the next section.

2.2 Diagonal Preconditioner

The scalar preconditioners described above do not combat the more serious stiffness arising from large cell aspect ratios and the disparity in propagative speeds within the systems. Although these are two separate issues, effective treatment for each depends on operating on the appropriate modal components of the solution. This realization motivated van Leer to introduce the notion of characteristic time stepping for the Euler equations, with the aim of limiting the evolution of each characteristic mode by the corresponding propagative speed [19].

Exact characteristic time stepping is only possible in 1D, where the system may be decoupled into scalar characteristic equations using an eigenvector decomposition of the single flux Jacobian. In multiple dimensions, the flux Jacobians cannot be simultaneously diagonalized, so Lee and van Leer designed a local matrix preconditioner intended to obtain a condition number as close to unity as possible [11, 20]. The resulting stream-aligned implementation is incompatible with standard mesh-aligned numerical dissipation and becomes fragile near stagnation points where the flow direction is not well-defined. A more substantial limitation of this approach is that the objective of obtaining a unit condition number for the propagative speeds does not take into account the stiffness arising from high aspect ratio cells in a typical computational mesh. As a result, extension to Navier–Stokes applications is problematic.

The following diagonal Euler preconditioner represents an intuitive approach to approximate characteristic time stepping on stretched meshes in which $\Delta y \ll \Delta x$. A straightforward extension to the Navier–Stokes equations is also provided. Following Lee and van Leer, the "entropy" variables defined by $d\widetilde{W} = \{\frac{dp}{\rho c}, du, dv, dp - c^2 d\rho\}^T$ are used to simultaneously symmetrize and greatly simplify the flux Jacobians. The first and third variables are associated with predominantly acoustic modes since a pressure wave front traveling outward from a wall at $y = 0$ perturbs the pressure field and the perpendicular velocity field. These modes should both be limited by the standard hyperbolic time step (2.5),

$$\Delta\widetilde{t}_p^{-1} = \Delta\widetilde{t}_v^{-1} = \frac{1}{\mathrm{CFL_H}} \left(\frac{|u|+c}{\Delta x} \; + \; \frac{|v|+c}{\Delta y} \right) .$$

The second variable is associated with a streamwise convection mode supplemented by the sonic speed and need not be limited by the sonic speed in the transverse direction

$$\Delta\widetilde{t}_u^{-1} = \frac{1}{\mathrm{CFL_H}} \left(\frac{|u|+c}{\Delta x} \; + \; \frac{|v|}{\Delta y} \right) .$$

The fourth variable is completely decoupled from the other three and represents a convective entropy mode which need not be limited by the sonic speed in either direction

$$\Delta\widetilde{t}_s^{-1} = \frac{1}{\mathrm{CFL_H}} \left(\frac{|u|}{\Delta x} \; + \; \frac{|v|}{\Delta y} \right) .$$

The diagonal Euler preconditioner in entropy variables takes the form

$$P_{D_E}^{-1} = \mathrm{diag}[\Delta\widetilde{t}_p^{-1}, \Delta\widetilde{t}_u^{-1}, \Delta\widetilde{t}_v^{-1}, \Delta\widetilde{t}_s^{-1}].$$

A simple extension to the Navier–Stokes equations is possible by incorporating P_{D_E} into the same stability requirement used for the scalar time step (2.4), so that the Navier–Stokes preconditioner is given by

$$P_{D_{NS}}^{-1} = P_{D_E}^{-1} + \Delta t_P^{-1} I,$$

where I is the identity matrix and the parabolic time step Δt_P is defined by (2.6).

For a semi-discrete scheme, the updating procedure then becomes

$$\frac{dW}{dt} + NP_D N^{-1} R(W) = 0\,,$$

where $N = \frac{\partial W}{\partial \widetilde{W}}$ and $N^{-1} = \frac{\partial \widetilde{W}}{\partial W}$ represent transformations between conservative and symmetrizing variables. Because the implementation is mesh-aligned, no alteration of the dissipation is required and no ambiguity arises near stagnation points [15].

It is essential to note that characteristic time stepping is only possible in conjunction with characteristic-based rather than scalar numerical dissipation. This may be understood by considering the necessary and sufficient stability condition for the scalar advection-diffusion equation

$$u_t + a u_x = \nu u_{xx}$$

discretized using central differences in space and forward differences in time

$$\Delta t \leq \min\left(\tfrac{2\nu}{a^2}, \tfrac{\Delta x^2}{2\nu}\right)\,.$$

For 1st order upwinding, $\nu = \frac{|a|\Delta x}{2}$, and this requirement reduces to the standard CFL condition $\Delta t \leq \frac{\Delta x}{|a|}$. The corresponding representation of the Euler equations with characteristic-based matrix dissipation is

$$W_t + AW_x = \tfrac{\Delta x}{2}|A|W_{xx}.$$

Using a characteristic time step corresponds to decoupling the system into scalar characteristic equations

$$\Omega_t + \Lambda\Omega_x = \tfrac{\Delta x}{2}|\Lambda|\Omega_{xx}$$

using an eigenvector decomposition of the flux Jacobian $A = T\Lambda T^{-1}$ to produce the characteristic variables $\partial\Omega = T^{-1}\partial W$, where Λ is a diagonal eigenvalue matrix. Applying the advection-diffusion stability requirement separately to each characteristic equation leads to the limit $\Delta t_k \leq \frac{\Delta x}{|\lambda_k|}$ for the k-th characteristic, where λ_k is the corresponding eigenvalue. Therefore, every characteristic wave is evolving at its stability limit.

The Euler equations with standard scalar dissipation take the form

$$W_t + AW_x = \tfrac{\Delta x}{2}\rho(A)W_{xx},$$

where $\rho(A)$ is the spectral radius of the flux Jacobian. Using a characteristic time step, this system can still be decoupled into characteristic equations using the same transformation as above. However, the stability requirement for all characteristics is now just the standard scalar CFL condition, $\Delta t_k \leq \frac{\Delta x}{\rho(A)}$, so the advantage of a characteristic time step is lost.

One possibility for avoiding the added expense of matrix dissipation while still satisfying the stability requirement for a characteristic time step is the scalar CUSP splitting proposed by Jameson, which actually introduces less dissipation than a standard characteristic upwind scheme [9, 18].

2.3 Block-Jacobi Preconditioner

For multigrid to function efficiently, the relaxation scheme on each mesh must damp all modes which cannot be resolved without aliasing on the next coarser mesh in the cycle. For a multi-stage Runge-Kutta time stepping scheme, this corresponds to clustering the eigenvalues of the residual away from the origin in Fourier space. In a recent paper, Allmaras examined the necessary damping requirements for relaxation methods used to drive both full and semi-coarsening multigrid algorithms [2].

For full coarsening multigrid, the relaxation scheme must damp all modes which are high frequency in either mesh direction since only those modes which are low frequency in both directions can be resolved on the next coarser grid. Explicit relaxation methods are notoriously ineffective in damping modes which are high frequency in one direction and low frequency in the other, which led Allmaras to propose implicit ADI relaxation for use with full coarsening multigrid [2].

The semi-coarsening algorithm proposed by Mulder [13, 14] coarsens separately in each mesh direction and therefore reduces the region of Fourier space for which the relaxation scheme on each mesh must successfully damp modes for the algorithm to function efficiently. To obtain an $O(N)$ method for a 3D mesh with N points, Mulder defined a restriction and prolongation structure in which not all grids are coarsened in every direction. For 2D grids that are coarsened separately in both directions, only those modes which are high frequency in both mesh directions need by damped by the relaxation scheme. For this purpose, Allmaras suggests a point-implicit block-Jacobi preconditioner that has previously been demonstrated to be effective in clustering high frequency eigenvalues away from the origin [1]. For grids that are not coarsened in one of the mesh directions, Allmaras proposes using a semi-implicit line-Jacobi preconditioner in that direction [2].

These strategies for preconditioning in the context of both full and semi-coarsening multigrid are well-conceived. The drawback to implicit ADI preconditioning for full coarsening multigrid is the increased complexity in developing parallel implementations. The semi-coarsening strategy is actually better in this regard, since most of the work is performed on meshes for which a point-implicit preconditioner is sufficient. However, the drawback is that for a 3D computation, the cost of a full coarsening W cycle is bounded by $\frac{4}{3}N$, while a semi-coarsening W cycle is no longer $O(N)$ and the bounds for V and F cycles are $8N$ and $32N$, respectively [7, 13]. None the less, the improved performance may justify the additional cost if full coarsening multigrid results cannot be sufficiently improved.

For the time being, it is worthwhile determining whether an explicit or point-implicit preconditioner that is easily parallelized can be used in conjunction with inexpensive full coarsening multigrid to produce significant convergence improvements for practical aerodynamic computations. With this in mind, the properties and performance of the point-implicit block-Jacobi preconditioner are examined in the present work.

For a preconditioned semi-discrete scheme of the form (2.1), the residual for a standard spatial discretization incorporating a 2nd/4th difference switch of the type introduced by Jameson *et al.* [10] applied to Roe-averaged characteristic variables

[16], takes the form

$$\begin{aligned} R &= \tfrac{A}{2\Delta x}\delta_{2x} - (S_x)\tfrac{|A|}{2\Delta x}\delta_{xx} + (1-S_x)\varepsilon^{(4)}\tfrac{|A|}{\Delta x}\delta_{xxxx} \\ &+ \tfrac{B}{2\Delta y}\delta_{2y} - (S_y)\tfrac{|B|}{2\Delta y}\delta_{yy} + (1-S_y)\varepsilon^{(4)}\tfrac{|B|}{\Delta y}\delta_{yyyy} \\ &- \tfrac{C}{\Delta x^2}\delta_{xx} - \tfrac{D}{\Delta y^2}\delta_{yy} - \tfrac{E}{4\Delta x\Delta y}\delta_{2x2y}, \end{aligned} \tag{2.7}$$

where S is a switch taking values between zero and one.

The block-Jacobi preconditioner is obtained by extracting the elements of the residual operator which correspond to the central node

$$P^{-1}_{J_{NS}} = \tfrac{1}{\mathrm{CFL_H}}\left\{[S_x + 6\varepsilon^{(4)}(1-S_x)]\tfrac{|A|}{\Delta x} + [S_y + 6\varepsilon^{(4)}(1-S_y)]\tfrac{|B|}{\Delta y} + \tfrac{2C}{\Delta x^2} + \tfrac{2D}{\Delta y^2}\right\}.$$

From this expression it is apparent that for a fourth difference dissipation coefficient of $\varepsilon^{(4)} = \frac{1}{6}$, the block-Jacobi preconditioner is identical for both 2nd and 4th differences. In practice, this is found to be a very suitable coefficient for matrix characteristic-based dissipation, though it would be far too dissipative for a scalar scheme. The simplified block-Jacobi preconditioner for the 2D Navier–Stokes equations may therefore be written

$$P^{-1}_{J_{NS}} = \tfrac{1}{\mathrm{CFL_H}}\left(\tfrac{|A|}{\Delta x} + \tfrac{|B|}{\Delta y} + \tfrac{2C}{\Delta x^2} + \tfrac{2D}{\Delta y^2}\right).$$

In this form it is equally suitable for both smooth and shocked regions of the flow, where the two different types of numerical dissipation are active. The block-Jacobi preconditioner for the 2D Euler equations is obtained by eliminating the viscous terms

$$P^{-1}_{J_E} = \tfrac{1}{\mathrm{CFL_H}}\left(\tfrac{|A|}{\Delta x} + \tfrac{|B|}{\Delta y}\right).$$

The necessity of matrix dissipation for use in conjunction with the block-Jacobi preconditioners is obvious since they reduce to scalar preconditioners by identity using standard scalar dissipation based on the spectral radii of the flux Jacobians.

3 Analysis

3.1 Fourier Footprints and Wave Front Envelopes

For a semi-discrete scheme (2.1), the Fourier footprint of the spatial discretization is critical in determining the effectiveness of a multi-stage time stepping scheme in damping error modes. The footprint is found by substituting a semi-discrete Fourier mode of the form

$$W_{j,k} = \widehat{W}(t)e^{i(j\theta_x + k\theta_y)}$$

into the discrete residual operator (2.7). The Fourier amplitude $\widehat{W}(t)$ satisfies the evolution equation

$$\tfrac{d\hat{W}}{dt} + PZ\widehat{W} = 0,$$

where Z is the Fourier symbol of the residual operator

$$\begin{aligned} Z(\theta_x,\theta_y) &= i\tfrac{A}{\Delta x}\sin\theta_x + (S_x)\tfrac{|A|}{\Delta x}(1-\cos\theta_x) + (1-S_x)4\varepsilon^{(4)}\tfrac{|A|}{\Delta x}(1-\cos\theta_x)^2 \\ &+ i\tfrac{B}{\Delta y}\sin\theta_y + (S_y)\tfrac{|B|}{\Delta y}(1-\cos\theta_y) + (1-S_y)4\varepsilon^{(4)}\tfrac{|B|}{\Delta y}(1-\cos\theta_y)^2 \\ &+ \tfrac{2C}{\Delta x^2}(1-\cos\theta_x) + \tfrac{2D}{\Delta y^2}(1-\cos\theta_y) + \tfrac{E}{\Delta x\Delta y}\sin\theta_x\sin\theta_y\,. \end{aligned} \tag{3.1}$$

The Fourier footprint is obtained numerically by computing the eigenvalues of PZ for the desired range of (θ_x, θ_y). For stability, the footprint must lie within the stability region of the time stepping scheme defined by $|\psi(z)| \leq 1$, where $\psi(z)$ is the amplification factor defined by

$$\widehat{W}^{n+1} = \psi(z)\widehat{W}^n.$$

Assuming constant Pr and γ, the four independent parameters that govern the discrete Navier–Stokes residual are the cell Reynolds number, Mach number, cell aspect ratio and flow angle:

$$Re_\square = \frac{u\Delta x + v\Delta y}{\nu}, \quad M = \frac{\sqrt{u^2+v^2}}{c}, \quad \frac{\Delta y}{\Delta x}, \quad \frac{v}{u} \ .$$

The flow angle does not play a particularly interesting role in determining the form of the residual and is taken to be zero or asymptotically zero in all of the cases examined. As a result, the cell Reynolds number is actually the Reynolds number based on Δx: $Re_\square = Re_{\Delta x}$. All residuals that incorporate 4th difference matrix dissipation use a dissipation coefficient $\varepsilon^{(4)} = \frac{1}{6}$. Following from the discussion in Section 2.3, the effect of these preconditioners will only be examined for modes which are high frequency in both mesh directions ($\frac{\pi}{2} \leq \theta_x, \theta_y \leq \pi$).

Fourier footprints of high frequency modes for all Mach regimes $M = (0.05,\ 0.5,\ 0.95,\ 2.0)$ and the parameters $\frac{\Delta y}{\Delta x} = \frac{1}{5}$, $\frac{v}{u} = 0$ and $Re_{\Delta x} = \infty$ are displayed on the left hand side of Figs 1-4 for each of the three preconditioners. The outer solid line represents the stability region for Martinelli's 5-stage Runge-Kutta scheme and is superimposed to assist in determining appropriate choices for the hyperbolic and parabolic CFL numbers [12]. For these cases, $Re_{\Delta x} = \infty$, so that the preconditioners contain only the hyperbolic CFL number. For Navier–Stokes calculations, the fact that the maximum extent along the negative real axis is roughly twice the extent in either direction along the imaginary axis suggests the definition $\mathrm{CFL_P} = 2\mathrm{CFL_H}$, so that only the hyperbolic CFL number need be determined and the subscript may be dropped. The inner solid line represents the optimal clustering envelope for high frequency modes based on a scalar advection-diffusion model problem [1].

In Fig. 1, the Fourier footprint for low subsonic flow is shown for 2nd difference (1st order upwind) matrix dissipation and CFL = 2.5. The corresponding damping histograms displayed on the right hand side of the page show the fraction of eigenvalues with amplification factor $\psi(z)$ for a set of discrete ranges on the interval (0,1). In 2D there are four characteristic families representing convective entropy and vorticity modes and two acoustic pressure modes. The scalar preconditioner is unable to cluster the eigenvalues for the entropy mode away from the origin, so that exactly a quarter of the values in the damping histogram are concentrated very near an amplification factor of one. All three preconditioners are relatively effective at clustering the eigenvalues corresponding to the two acoustic modes away from the origin. The treatment of the entropy mode by the diagonal and block-Jacobi preconditioners is identical, with the eigenvalues forming an arc on the optimal clustering envelope.

For the Euler equations, additional information may be gained by examining the effect of the preconditioners on the shape of the wave front envelopes of the four characteristic families, as observed by van Leer and Lee [20, 11]. The propagative speed for a wave traveling at an angle $\theta = \tan^{-1}\frac{y}{x}$ is given for each of the four

characteristic families by an eigenvalue of the matrix

$$P(A\cos\theta + B\sin\theta).$$

The wave front for each eigenvalue is the line perpendicular to the direction of propagation. The wave front envelope for a family of waves is formed by the intersection of all the wave fronts in that family. Wave front envelopes for three different Mach numbers are displayed on the right hand side of Figs 2-4.

Fig. 2 shows the Fourier footprint for 4th difference matrix dissipation at $M = 0.5$ with CFL = 2.5. It is satisfactory that the same CFL number is suitable for both the 1st order upwind and 4th difference dissipation so that neither type is limited by the other when they are both active on the finest mesh in the multigrid cycle. For the scalar preconditioner, the entropy and vorticity wave fronts collapse to a point convecting with the flow and the two acoustic wave fronts form a circle centered on this point. These flow conditions provide a typical example of the transverse acoustic mode limiting the time step when the flow is aligned with a stretched mesh cell. As a result, the eigenvalues corresponding to the convective modes are close to the origin and cannot be rapidly damped.

The wave front envelopes of the diagonal and block-Jacobi preconditioners are surprisingly similar. Both have succeeded in moving the entropy envelope out to its maximum stability limit at 2.5 on the real axis. This corresponds to an optimal Fourier footprint based on the scalar model problem. Furthermore, in both cases, the acoustic envelopes have become elongated in the direction of cell stretching and the vorticity envelope extends away from the origin with a triangular shape. The Fourier footprints for the acoustic modes have nearly the same radius as the entropy mode, one each above and below the real axis, with the vorticity mode forming a tongue between them. Note that the objective of the preconditioning is not to achieve a unit condition number, for which all wave front envelopes would fall on a circle of the same radius, as with the work of van Leer *et al.* [20]. Instead, the intent is to shape the wave front envelopes to approximate the cell aspect ratio, so that even on a highly stretched mesh, all disturbances cross the same number of cells per unit time regardless of the direction of propagation.

Footprints and envelopes for $M = 0.95$ and $M = 2.0$ are shown in Figs 3 and 4 for 4th difference matrix dissipation and CFL = 2.5. The footprints keep the same basic structure as for the previous two cases. The only change in the envelopes for the scalar and diagonal preconditioners is the shifting along the x axis as the convective component of the acoustic speed increases. However, the behavior of the block-Jacobi preconditioner changes completely for the transonic and supersonic regimes. The vorticity envelope converges on the same optimal point as the entropy envelope and the acoustic envelopes collapse to two points on the Mach waves, which are shown by dotted lines for the supersonic case.

In each of these cases, the scalar preconditioner is unsuccessful in clustering the eigenvalues of the convective modes away from the origin, although the deleterious effects of this shortcoming are mitigated as the Mach number increases. Clustering for the acoustic modes is satisfactory, though sub-optimal. The diagonal preconditioner provides optimal clustering for the entropy mode and satisfactory but sub-optimal clustering for the acoustic and vorticity modes. By contrast, the block-Jacobi preconditioner successfully clusters the eigenvalues of all four modes inside the optimal

Case 1	$Re_{\Delta x} = \infty$	$M \to 0$	$\frac{\Delta y}{\Delta x} \to 0$	$\frac{v}{u} = \frac{\Delta y}{\Delta x}$
Case 2	$Re_{\Delta x} = \infty$	$M \to 0$	$\frac{\Delta y}{\Delta x} \to 0$	$\frac{v}{u} = 0$
Case 3	$Re_{\Delta x} = \infty$	$M \to 0$	$\frac{\Delta y}{\Delta x} \to \infty$	$\frac{v}{u} = 0$
Case 4	$Re_{\Delta x} = \infty$	$M = 0.5$	$\frac{\Delta y}{\Delta x} \to \infty$	$\frac{v}{u} = 0$
Case 5	$Re_{\Delta x} \to \infty$	$M \to 0$	$\frac{\Delta y}{\Delta x} = Re_{\Delta x}^{-1/2}$	$\frac{v}{u} = 0$
Case 6	$Re_{\Delta x} \to \infty$	$M = 0.5$	$\frac{\Delta y}{\Delta x} = Re_{\Delta x}^{-1/2}$	$\frac{v}{u} = 0$

Table 1: Asymptotic limits used to obtain analytic expressions for the Fourier footprint of 4th difference matrix dissipation.

envelope for each case. This is not necessarily the case for block-Jacobi preconditioning of the Navier–Stokes equations as a result of the viscous cross-derivative term.

3.2 Analytic Asymptotic Results

Having considered these rather moderate flow conditions, it is now worthwhile examining the behavior of the preconditioned system in more extreme conditions typical of a viscous boundary layer, where the greatest stiffness is generally encountered. Analytic expressions for the preconditioned Fourier footprints are obtained for the important set of asymptotic limits summarized in Table 1. Cases 1-4 assume $Re_{\Delta x} = \infty$, so that the viscous terms are neglected, though the effect of an "inviscid" boundary layer is simulated for the first three cases by letting $M \to 0$. Case 1 corresponds to a stretched cell with diagonal cross flow. Case 2 represents a stretched cell with aligned flow. Case 3 is a cell stretched perpendicular to the flow, as occurs at the leading edge of an airfoil. Case 4 examines a moderate subsonic flow perpendicular to a highly stretched cell. This situation often occurs in the far field due to exponential stretching of the transverse mesh coordinates. Cases 5 and 6 consider the asymptotic behavior for stretched cells in a viscous boundary layer. The scaling for the cell aspect ratio is found by balancing streamwise convection and normal diffusion, so that

$$\frac{u}{\Delta x} = \frac{\nu}{\Delta y^2} ,$$

which leads to the relation

$$\frac{\Delta y}{\Delta x} = Re_{\Delta x}^{-1/2} .$$

To simplify the analysis for Cases 5 and 6, the Prandtl number is assumed to be unity. All of the cases are analyzed for 4th difference matrix dissipation, since this is the type that is active over most of the fine mesh. The dissipative coefficient is taken to be $\varepsilon^{(4)} = \frac{1}{6}$ with CFL = 1.0.

The analytic asymptotic limits of the eigenvalue distributions for all six cases are shown in Table 2, where the notation $s_x \equiv \sin\theta_x$, $s_y \equiv \sin\theta_y$, $C_x \equiv 1 - \cos\theta_x$, $C_y \equiv 1 - \cos\theta_y$ is adopted for brevity. The corresponding Fourier footprints for the high frequency modes are plotted in Figs 5-7 using a separate symbol for each family, as defined in Table 3. This table describes the asymptotic dependences of

the different families on the two Fourier angles, corresponding to the directions of effective smoothing.

Using the scalar preconditioner, both convective modes fall on the origin for every case except the subsonic cross flow of Case 4, when three of the modes form a version of the optimal envelope scaled by a factor of $\frac{1}{3}$. By examining Table 3 it is evident that the eigenvalues for the acoustic modes are dominated by the normal component for aligned or nearly aligned flow and the streamwise component for cross flow.

The diagonal preconditioner succeeds in clustering all the eigenvalues inside the optimal envelope for Cases 1, 2 and 5, all of which represent aligned or nearly aligned flow with vanishing Mach number. For Case 3, the vorticity mode collapses to the origin, which is a major drawback since this flow condition is encountered near stagnation points. For Case 4, the vorticity mode and one acoustic mode fall on the same reduced version of the optimal envelope as for the scalar preconditioner. For Case 6, only a small fraction of the vorticity eigenvalues are not clustered inside the optimal envelope.

The block-Jacobi preconditioner succeeds in clustering all eigenvalues inside the optimal envelope for both inviscid and viscous asymptotic limits. The footprints for Cases 1 and 2 are identical to those for the diagonal preconditioner. The handling of Cases 3 and 4 is much improved over that of the diagonal preconditioner, while the treatment of Cases 5 and 6 is remarkably similar, as seen by examining the analytic expressions in Table 2.

In general, the scalar preconditioner is unacceptable for highly stretched cells either aligned or perpendicular to the flow. The diagonal preconditioner performs well when the flow is nearly aligned with a stretched mesh but breaks down when there is a strong cross flow. The block-Jacobi preconditioner, on the other hand, performs optimally for every case.

The performance of the preconditioners on modes which are high frequency in one direction and low frequency in the other is revealed by examining Table 3. Asymptotic dependence on a Fourier angle amounts to effective damping of modes in that direction, since the corresponding eigenvalues will not be clustered at the origin. For the viscous conditions of Cases 5 and 6, none of the preconditioners are able to cope with a sawtooth pressure mode in the streamwise direction, but both matrix preconditioners are able to damp entropy modes in either direction, even for perfectly aligned flow. Notice that this is not the case for the inviscid aligned flow of Case 2, where a normal sawtooth entropy mode will not be damped in a highly stretched cell.

4 Results

Results for a number of standard airfoil test cases are generated using a conservative cell-centered semi-discrete finite volume scheme. Characteristic-based matrix dissipation based on Roe's linearization [16] provides a basis for the construction of high resolution switched, symmetric limited and upstream limited schemes following the work of Jameson [10, 5, 6, 8]. Updates are performed using a 5-stage Runge-Kutta time stepping scheme to drive a full coarsening multigrid algorithm [10, 3, 12]. The solution is computed on a sequence of fine meshes using a W-cycle on each mesh. A single time step is performed at each level when moving down the multigrid cycle.

Case	$-\text{eig}(P_S Z)$	$-\text{eig}(P_D Z)$	$-\text{eig}(P_J Z)$
1	0	$\frac{1}{2}[\frac{2}{3}(C_x^2+C_y^2)+i(s_x+s_y)]$	$\frac{1}{2}[\frac{2}{3}(C_x^2+C_y^2)+i(s_x+s_y)]$
	0	$\frac{2}{3}C_x^2$	$\frac{2}{3}C_x^2$
	$\frac{2}{3}C_y^2+is_y$	$\frac{2}{3}C_y^2+is_y$	$\frac{2}{3}C_y^2+is_y$
	$\frac{2}{3}C_y^2-is_y$	$\frac{2}{3}C_y^2-is_y$	$\frac{2}{3}C_y^2-is_y$
2	0	$\frac{2}{3}C_x^2+is_x$	$\frac{2}{3}C_x^2+is_x$
	0	$\frac{2}{3}C_x^2$	$\frac{2}{3}C_x^2$
	$\frac{2}{3}C_y^2+is_y$	$\frac{2}{3}C_y^2+is_y$	$\frac{2}{3}C_y^2+is_y$
	$\frac{2}{3}C_y^2-is_y$	$\frac{2}{3}C_y^2-is_y$	$\frac{2}{3}C_y^2-is_y$
3	0	$\frac{2}{3}C_x^2+is_x$	$\frac{2}{3}C_x^2+is_x$
	0	0	$\frac{1}{2}[\frac{2}{3}(C_x^2+C_y^2)+is_x]$
	$\frac{2}{3}C_x^2+is_x$	$\frac{2}{3}C_x^2+is_x$	$\frac{2}{3}C_x^2+is_x$
	$\frac{2}{3}C_x^2-is_x$	$\frac{2}{3}C_x^2-is_x$	$\frac{2}{3}C_x^2-is_x$
4	$\frac{1}{3}(\frac{2}{3}C_x^2+is_x)$	$\frac{2}{3}C_x^2+is_x$	$\frac{2}{3}C_x^2+is_x$
	$\frac{1}{3}(\frac{2}{3}C_x^2+is_x)$	$\frac{1}{3}(\frac{2}{3}C_x^2+is_x)$	$\frac{2}{3}C_x^2+is_x$
	$\frac{2}{3}C_x^2+is_x$	$\frac{2}{3}C_x^2+is_x$	$\frac{2}{3}C_x^2+is_x$
	$\frac{1}{3}(\frac{2}{3}C_x^2-is_x)$	$\frac{1}{3}(\frac{2}{3}C_x^2-is_x)$	$\frac{2}{3}C_x^2-is_x$
5	0	$\frac{1}{1+2\gamma}(\frac{2}{3}C_x^2+2C_y+is_x)$	$\frac{1}{3}(\frac{2}{3}C_x^2+2C_y+is_x)$
	0	$\frac{2}{3}C_x^2$	$\frac{2}{3}C_x^2$
	$\frac{2}{3}C_y^2+is_y$	$\frac{2}{3}C_y^2+is_y$	$\frac{2}{3}C_y^2+is_y$
	$\frac{2}{3}C_y^2-is_y$	$\frac{2}{3}C_y^2-is_y$	$\frac{2}{3}C_y^2-is_y$
6	0	$\frac{1}{1+2\gamma}(\frac{2}{3}C_x^2+2C_y+is_x)$	$\frac{1}{3}(\frac{2}{3}C_x^2+2C_y+is_x)$
	0	$\frac{1}{3+2\gamma}(\frac{4}{3}C_x^2+2C_y+is_x)$	$\frac{1}{4}(\frac{4}{3}C_x^2+2C_y+is_x)$
	$\frac{2}{3}C_y^2+is_y$	$\frac{2}{3}C_y^2+is_y$	$\frac{2}{3}C_y^2+is_y$
	$\frac{2}{3}C_y^2-is_y$	$\frac{2}{3}C_y^2-is_y$	$\frac{2}{3}C_y^2-is_y$

Table 2: Analytic expressions for the Fourier footprint of 4th difference matrix dissipation with Scalar, Diagonal and Block-Jacobi preconditioning.

Mode	Entropy $(\cdot)$			Vorticity $(*)$			Acoustic $(\circ)$			Acoustic $(+)$		
Speed	q			q			$q+c$			$q-c$		
Precon	P_S	P_D	P_J	P_S	P_D	P_J	P_S	P_D	P_J	P_S	P_D	P_J
Case 1	0	θ_x, θ_y	θ_x, θ_y	0	θ_x	θ_x	θ_y	θ_y	θ_y	θ_y	θ_y	θ_y
Case 2	0	θ_x	θ_x	0	θ_x	θ_x	θ_y	θ_y	θ_y	θ_y	θ_y	θ_y
Case 3	0	θ_x	θ_x	0	0	θ_x, θ_y	θ_x	θ_x	θ_x	θ_x	θ_x	θ_x
Case 4	θ_x	θ_x	θ_x	θ_x	θ_x	θ_x	θ_x	θ_x	θ_x	θ_x	θ_x	θ_x
Case 5	0	θ_x, θ_y	θ_x, θ_y	0	θ_x	θ_x	θ_y	θ_y	θ_y	θ_y	θ_y	θ_y
Case 6	0	θ_x, θ_y	θ_x, θ_y	0	θ_x, θ_y	θ_x, θ_y	θ_y	θ_y	θ_y	θ_y	θ_y	θ_y

Table 3: Definition of mode symbols and representative propagative speeds for Figs 5-7, and the asymptotic dependence of each mode on θ_x and θ_y, corresponding to the directions of effective smoothing.

The stability limit on both fine and coarse meshes is CFL = 2.5 and the high resolution schemes are used only on the fine meshes. The meshes have an O-topology, with the far field located at 30 chords and dimensions 160×32 for Euler calculations and 320×64 for laminar Navier–Stokes calculations. The plotted residuals represent the rms change in density during one application of the time stepping scheme on the finest mesh in the multigrid cycle. Descriptions of the geometry, flow parameters, mesh properties, dissipative scheme and observed speedups for each test case are provided in Table 4. The speedups are calculated at a residual level of 10^{-4} based on an initial residual of unity. The additional cost of matrix preconditioning is 10-15% for diagonal and 20-25% for block-Jacobi if the preconditioner is updated once per time step.

4.1 Euler

The results for the design point of the KORN airfoil computed using a matrix switch are shown in Fig. 8. The pressure distribution is shock free with only two counts of drag. Convergence plots are shown for the high resolution solution and also for first order upwinding. The improvement in the performance of the diagonal preconditioner relative to the scalar preconditioner for the first order scheme is typical of most test cases. The maximum cell aspect ratio in the far field is 20 and the minimum cell aspect ratio at the wall is $\frac{1}{2}$, though the minimum height of the first cell is only 0.0005 chords.

In Fig. 9, solutions to a standard NACA0012 test case with a weak shock on the lower surface are shown after 12 and 100 W-cycles using a matrix switched scheme and block-Jacobi preconditioning. After 12 cycles, the lift changes by only four counts and the drag is fully converged. This rate of convergence is achieved with CFL = 2.5 and without implicit residual averaging or enthalpy damping [4]. Once again, the performance of the diagonal preconditioner on a high resolution scheme is disappointing.

The solution to a subsonic lifting NACA0012 test case is shown in Fig. 10. The prediction of a single count of drag is in close agreement with the theory for subsonic isentropic lifting flows. The diagonal preconditioner performance is midway between

Geometry	M_∞	α	Re_L	Mesh	$\left.\frac{\Delta\eta}{\Delta\xi}\right\|_{\max}$	$\left.\frac{\Delta\eta}{\Delta\xi}\right\|_{\min}$	$\left.\frac{\Delta\eta}{L}\right\|_{\text{wall}}$	Scheme	P_D	P_J
KORN	0.75	0.0°	∞	160×32	$2\times10^{+1}$	5×10^{-1}	5×10^{-4}	Switch	1.3	5.1
KORN	0.75	0.0°	∞	160×32	$2\times10^{+1}$	5×10^{-1}	5×10^{-4}	1st Up	1.9	3.6
NACA0012	0.8	1.25°	∞	160×32	$2\times10^{+1}$	5×10^{-1}	7×10^{-4}	Switch	1.2	3.7
NACA0012	0.5	3.0°	∞	160×32	$2\times10^{+1}$	5×10^{-1}	7×10^{-4}	Switch	1.7	2.9
NACA0012	1.2	0.0°	∞	160×32	$2\times10^{+1}$	5×10^{-1}	7×10^{-4}	Switch	1.0	4.0
NACA0012	1.2	0.0°	∞	320×64	$2\times10^{+1}$	5×10^{-1}	2×10^{-4}	Switch	1.0	14.3
Cylinder	0.38	0.0°	∞	128×48	$3\times10^{+0}$	1×10^{-1}	3×10^{-3}	Symlim	—	6.2
NACA0012	0.5	0.0°	5×10^{3}	320×64	$2\times10^{+1}$	5×10^{-1}	2×10^{-4}	Switch	1.5	2.0
NACA0012	0.5	0.0°	5×10^{3}	320×64	$2\times10^{+1}$	5×10^{-1}	2×10^{-4}	Symlim	1.5	2.1
NACA0012	0.8	10.0°	5×10^{2}	320×64	$2\times10^{+1}$	5×10^{-1}	2×10^{-4}	Switch	1.2	3.9
Flat Plate	0.15	0.0°	1×10^{5}	128×32	$4\times10^{+2}$	3×10^{-3}	3×10^{-5}	Switch	4.8	7.2

Table 4: Test case definitions, mesh dimensions, maximum and minimum cell aspect ratios, minimum ratio of cell height to chord length at the wall, dissipation type and speedups for P_D and P_J compared to P_S.

that of the scalar and block-Jacobi preconditioners.

Results for a symmetric supersonic test case are shown in Fig. 11. A 320×64 mesh was needed to adequately resolve the bow shock. Convergence comparisons are provided between the 320×64 mesh and a 160×32 mesh. The block-Jacobi preconditioner responds more favorably to the fine mesh than the other two preconditioners, which behave nearly identically on both meshes.

Fig. 12 displays the Mach contours for flow past a cylinder at $M_\infty = 0.38$ using matrix symmetric limited dissipation. The cell aspect ratio at the wall is $\frac{1}{10}$ and the first cells are 0.003 chords in height. The accuracy of the scheme is demonstrated by the symmetry of the solution upstream and downstream of the cylinder. The maximum entropy deviation in the cells next to the wall is 5×10^{-4}. No results are shown for the diagonal preconditioner, which did not converge due to an instability at the back stagnation point.

4.2 Laminar Navier–Stokes

Results for a subsonic laminar NACA0012 test case with $Re_L = 5000$ are shown in Fig. 13 for a 320×64 Euler mesh. The minimum height of the first cell is 0.0002, though the minimum cell aspect ratio is only $\frac{1}{2}$. Convergence comparisons are provided for both matrix switched and symmetric limited dissipation. The improvement of the diagonal and block-Jacobi preconditioners over the scalar preconditioner is about the same in each case. The budget plot for the x-momentum update across the boundary layer at the mid-chord reveals that the contribution of the numerical dissipation is negligible inside the boundary layer and also that the mesh resolution is insufficient for this Reynolds number.

Since the symmetric limited and switched formulations are fundamentally simi-

lar [8], it was expected that the block-Jacobi preconditioner based on the switched scheme would also be appropriate for symmetric limited dissipation. The results of Fig. 13 seem to confirm this hypothesis, recognizing that the reduction in convergence using symmetric limited dissipation is about the same for both scalar and matrix preconditioning. However, the speedups observed using an upstream limited scheme that does not resemble the 2nd/4th difference switching mechanism were also comparable, which suggests that it may be sufficient to base the form of the block-Jacobi preconditioner on the first order dissipative scheme. From this point of view, the principal advantage of reducing $\varepsilon^{(4)}$ to $\frac{1}{6}$ (from the more likely value of $\frac{1}{4}$), is the corresponding increase in the allowable time step from CFL = 1.8 to CFL = 2.5, which more than compensates for the reduced damping of the scheme. The footprint of the symmetric and upstream limited schemes is apparently larger than that of the switched scheme using either scalar or matrix preconditioning, since the CFL number could not be raised above 1.5 on the fine meshes.

Fig. 14 displays the results for a transonic laminar NACA0012 test case. The resolution of the mesh appears to be adequate for $Re_L = 500$ based on a comparison of the Mach number and pressure contours with results in [12]. This viewpoint is further supported by the budget plot at the lower midchord, which reveals that there are now roughly 20 points in the boundary layer. Once again, the block-Jacobi preconditioner realizes a significant speed-up over the standard scalar time step.

Results for nearly incompressible flow over a flat plate at $Re_L = 1{\times}10^5$ are displayed in Fig. 15 for a 128×32 H-mesh. Three quarters of the streamwise points are located on the plate and half the normal points are equally spaced in the boundary layer coordinate inside the boundary layer [17]. Exponential stretching is used in all directions outside the boundary layer, and some extremely high aspect ratio cells of $O(10^{\pm 5})$ are alleviated by skewing the stretching at the far field. It was necessary to reduce the CFL number to 2.0 on the fine meshes as a result of the extreme non-orthogonality in some cells. The maximum and minimum cell aspect ratios are 400 and $\frac{1}{330}$ and the minimum height of the first cell is 0.00003 chords. The inlet is one chord ahead of the plate, the outlet is at the trailing edge and the upper boundary is located two chords from the plate. A comparison of the velocity components at the mid-chord with the exact Blasius solution reveals a slight inaccuracy in the normal velocity component. Convergence plots are shown for both the density residual and the drag coefficient. The performance of all three preconditioners is in agreement with the analytic results for asymptotic boundary layer behavior, though the performance of the diagonal preconditioner is still somewhat surprising since there is a strong cross flow in all the far field cells. An examination of the residuals at the end of the three computations revealed that the convergence was dominated by the near field using a scalar preconditioner and the far field mesh singularity above the leading edge using the two matrix preconditioners.

5 Conclusions

Examination of the preconditioned wave front envelopes reveals that the basic structure does not vary significantly with Mach number for the scalar and diagonal preconditioners. The convective envelopes are limited by the circular acoustic envelopes in all cases using a scalar preconditioner. The diagonal preconditioner provides an optimal envelope for the decoupled entropy mode and the acoustic and vorticity envelopes are elongated in the direction of cell stretching. The block-Jacobi preconditioner shows the same behavior for subsonic flow, but for transonic flow the acoustic envelopes stretch normal to the flow and eventually collapse to points on the Mach angles when the flow becomes supersonic. Both the entropy and vorticity modes are located at the optimal stability limit for supersonic flow using a block-Jacobi preconditioner.

Analysis of the asymptotic behavior of the Fourier footprints for scalar, diagonal and block-Jacobi preconditioners reveals critical information about the successes and failures of these approaches. The scalar preconditioner is completely ineffective in clustering the high frequency convective modes away from the origin for all cases involving vanishing Mach number. The diagonal preconditioner performs well for all inviscid and viscous cases with aligned or nearly aligned flow but the performance deteriorates as the Mach number decreases for strong cross flow. Only the block-Jacobi preconditioner succeeds in clustering all high frequency modes inside the optimal envelope based on a scalar advection-diffusion model problem. However, the analysis seems to confirm the viewpoint of Allmaras that effectively damping high frequency modes with a point-implicit preconditioner and full coarsening multigrid may not be sufficient for stretched mesh computations. A less expensive alternative to full semi-coarsening is to semi-coarsen across the boundary layer until the cell aspect ratio approaches unity, at which point the residual eigenvalues of all modes will be dependent on both Fourier angles, and then adopt a full coarsening algorithm for the rest of each multigrid cycle.

Despite these reservations, very encouraging results have been achieved using full coarsening multigrid for a wide variety of Euler and laminar Navier–Stokes test cases using high resolution characteristic-based dissipation on fine meshes.

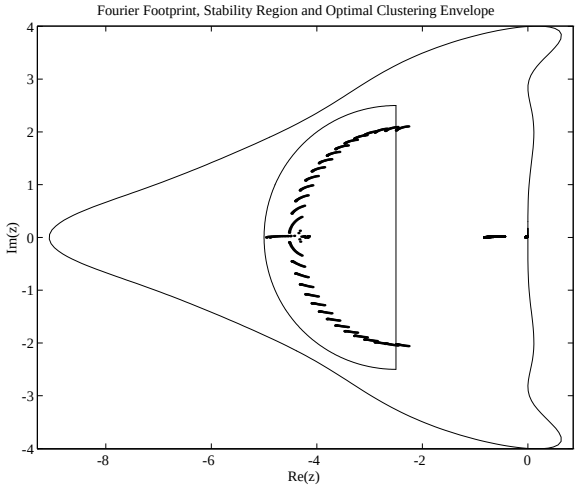

1a: Scalar Preconditioner.

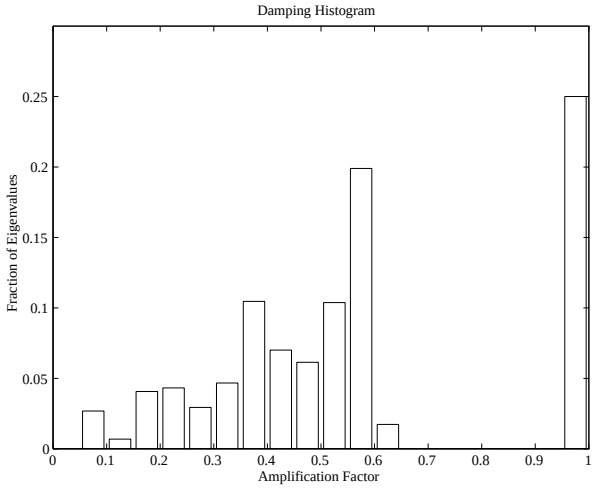

1b: Scalar Preconditioner.

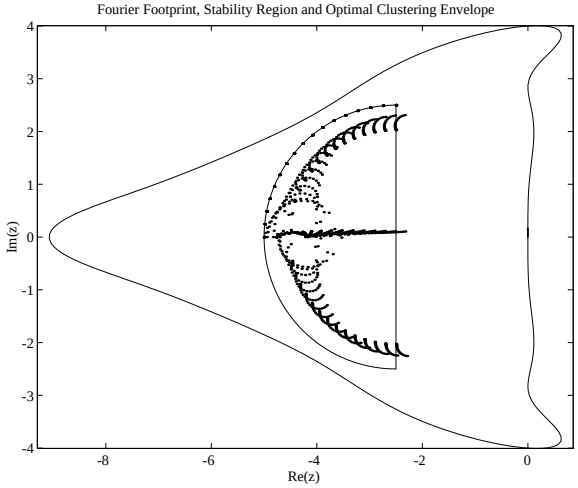

1c: Diagonal Preconditioner.

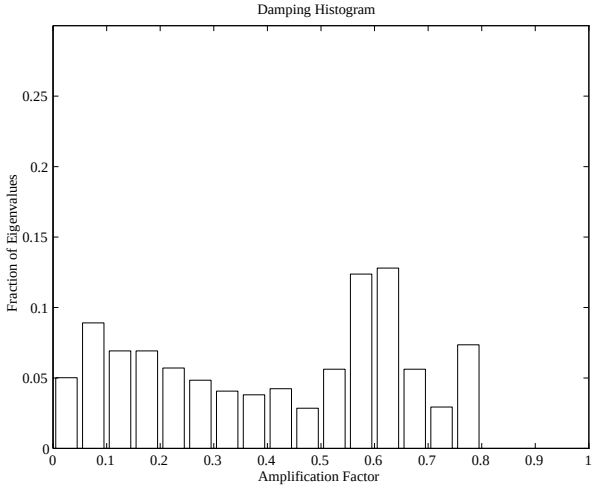

1d: Diagonal Preconditioner.

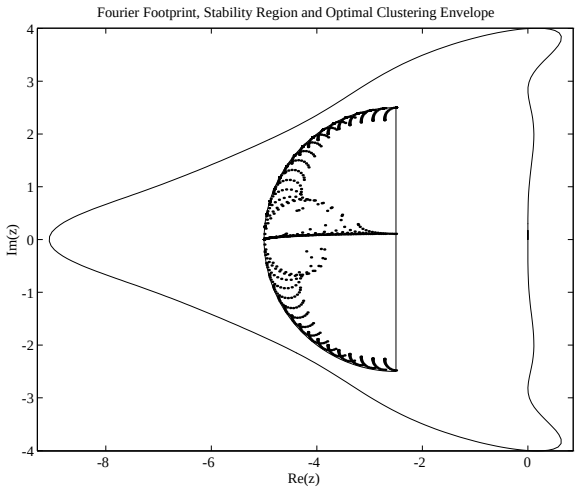

1e: Block-Jacobi Preconditioner.

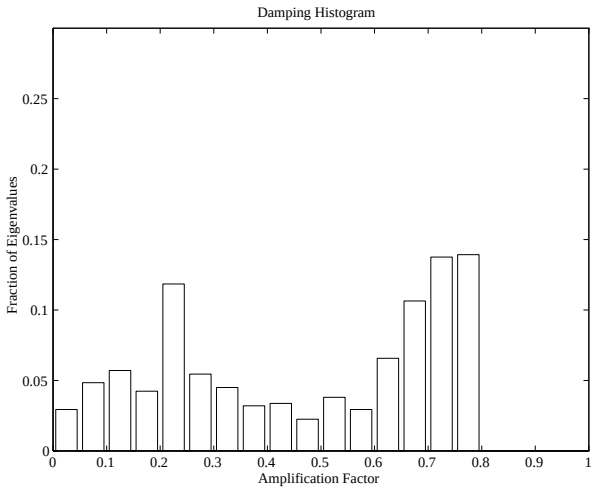

1f: Block-Jacobi Preconditioner.

Figure 1: 1st order upwind matrix dissipation.
Fourier footprint of high frequency modes and damping histogram for a 5-stage Runge-Kutta scheme.
$Re_{\Delta x} = \infty, M = 0.05, \frac{\Delta y}{\Delta x} = \frac{1}{5}, \frac{v}{u} = 0, \frac{\pi}{2} \leq \theta_x, \theta_y \leq \pi, \text{CFL} = 2.5.$

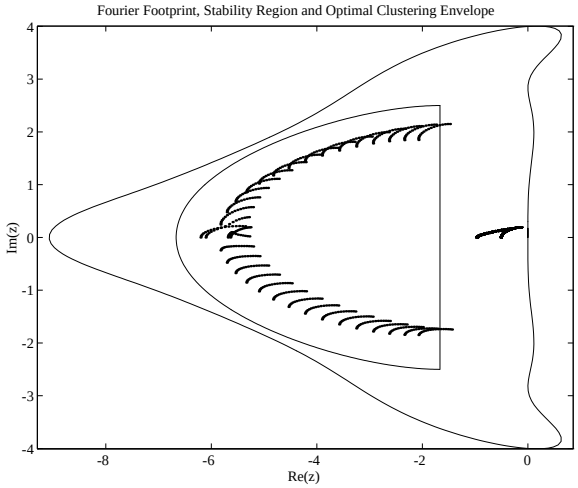

2a: Scalar Preconditioner.

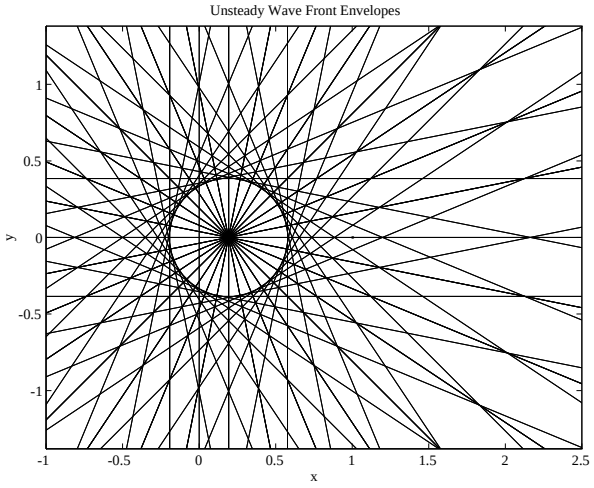

2b: Scalar Preconditioner.

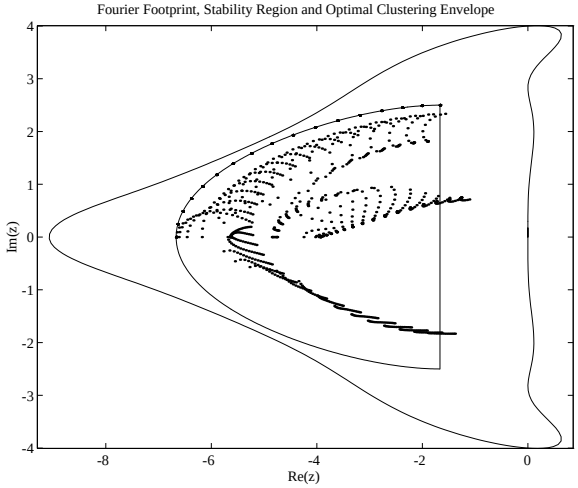

2c: Diagonal Preconditioner.

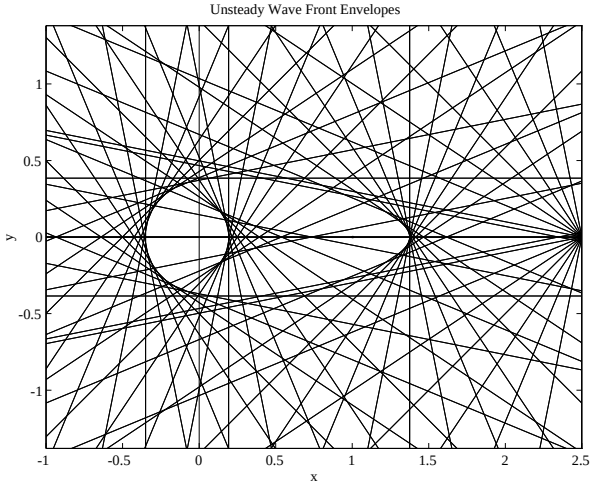

2d: Diagonal Preconditioner.

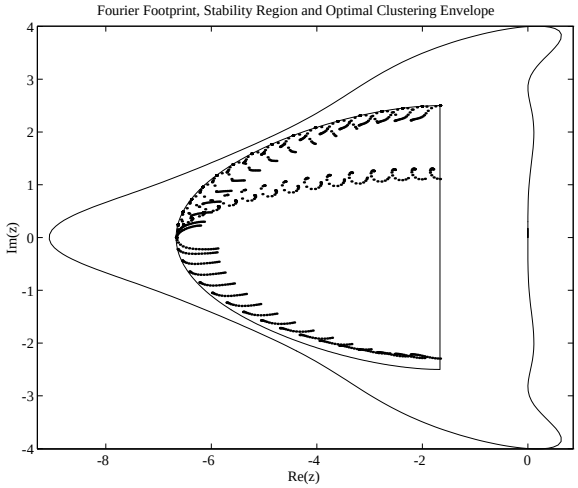

2e: Block-Jacobi Preconditioner.

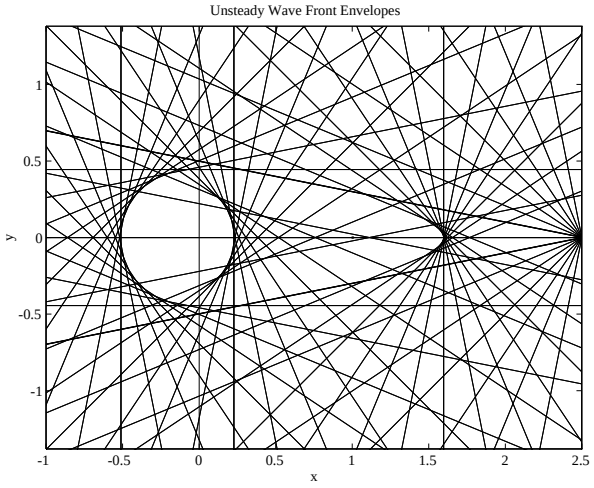

2f: Block-Jacobi Preconditioner.

Figure 2: 4th difference matrix dissipation.
Fourier footprint of high frequency modes and wave front envelopes.
$Re_{\Delta x} = \infty, M = 0.5, \frac{\Delta y}{\Delta x} = \frac{1}{5}, \frac{v}{u} = 0, \frac{\pi}{2} \leq \theta_x, \theta_y \leq \pi, \text{CFL} = 2.5.$

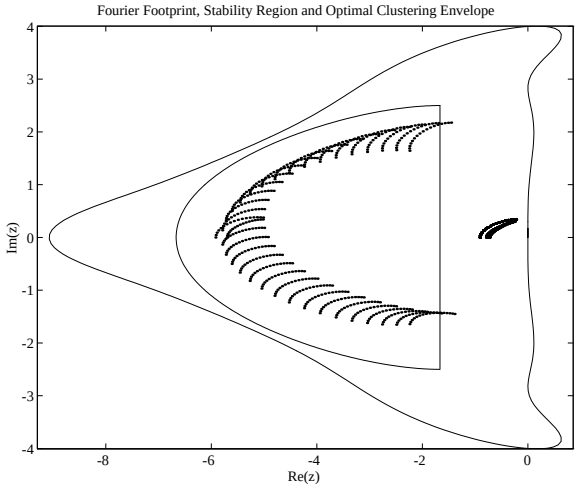

3a: Scalar Preconditioner.

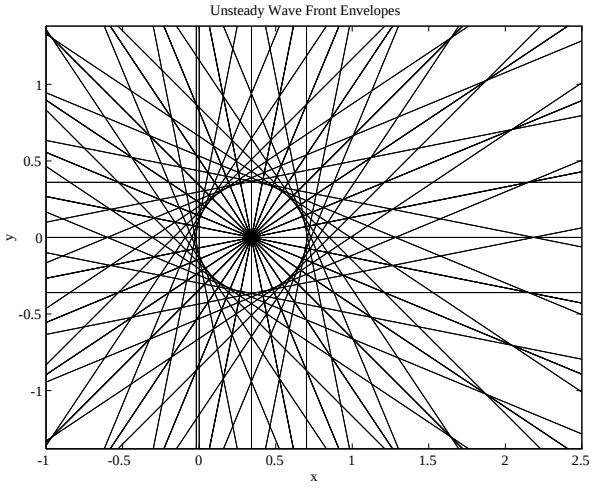

3b: Scalar Preconditioner.

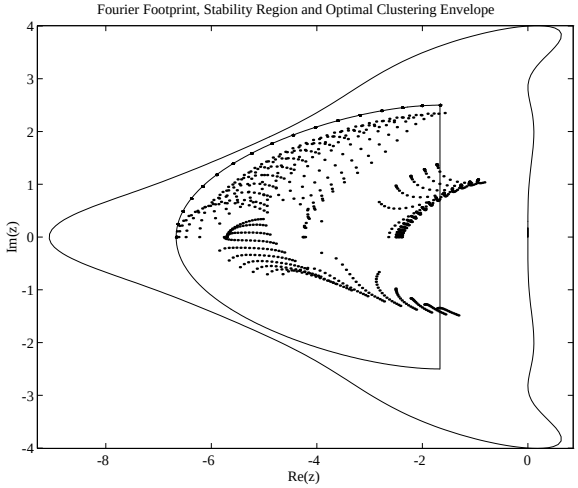

3c: Diagonal Preconditioner.

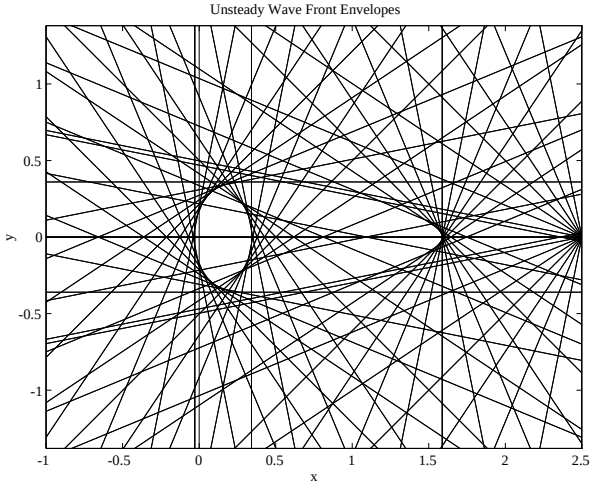

3d: Diagonal Preconditioner.

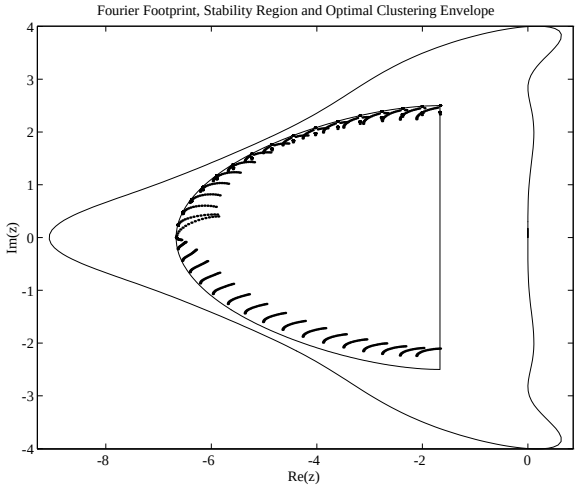

3e: Block-Jacobi Preconditioner.

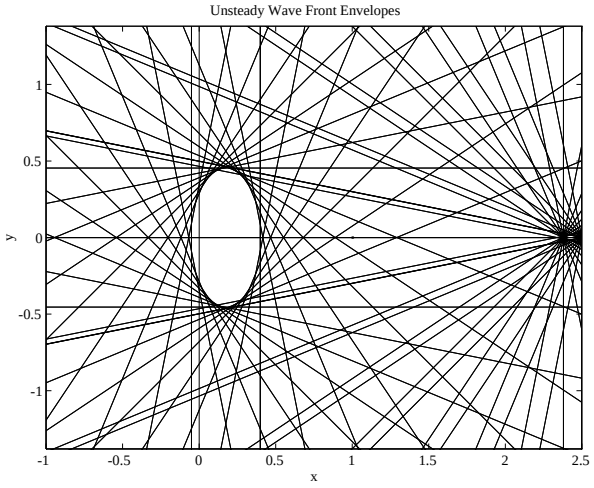

3f: Block-Jacobi Preconditioner.

Figure 3: 4th difference matrix dissipation.
Fourier footprint of high frequency modes and wave front envelopes.
$Re_{\Delta x} = \infty, M = 0.95, \frac{\Delta y}{\Delta x} = \frac{1}{5}, \frac{v}{u} = 0, \frac{\pi}{2} \leq \theta_x, \theta_y \leq \pi, \text{CFL} = 2.5.$

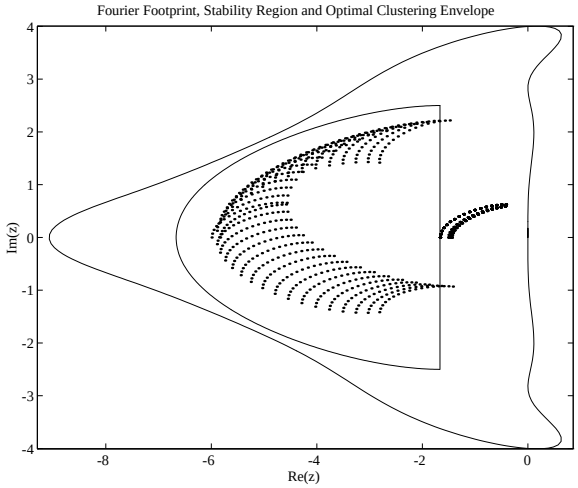

4a: Scalar Preconditioner.

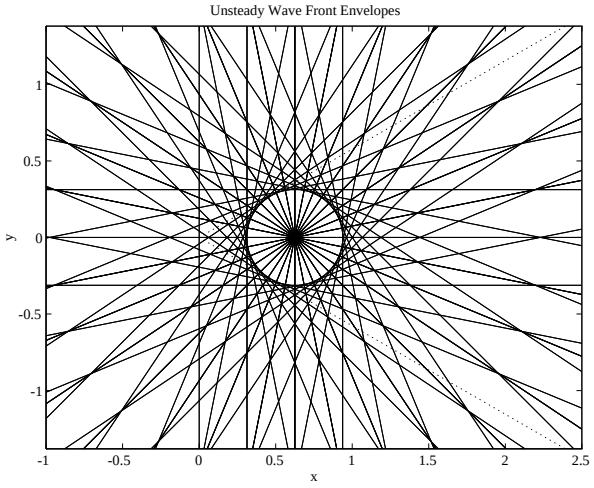

4b: Scalar Preconditioner.

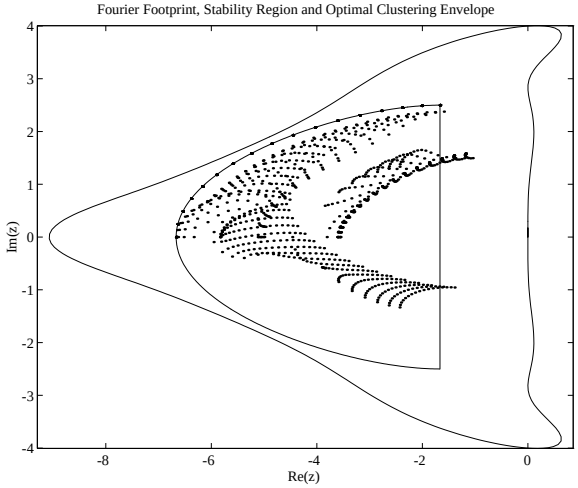

4c: Diagonal Preconditioner.

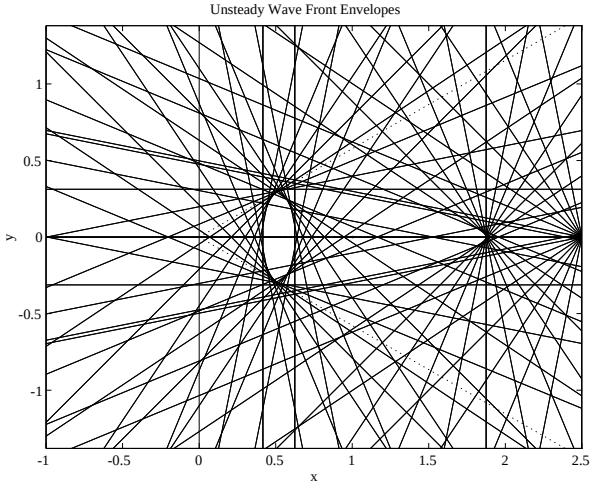

4d: Diagonal Preconditioner.

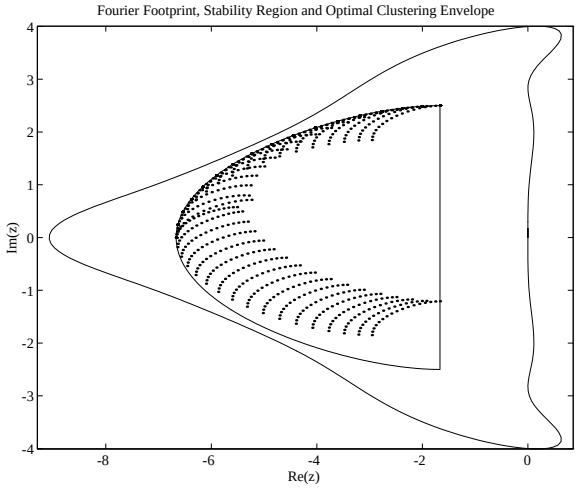

4e: Block-Jacobi Preconditioner.

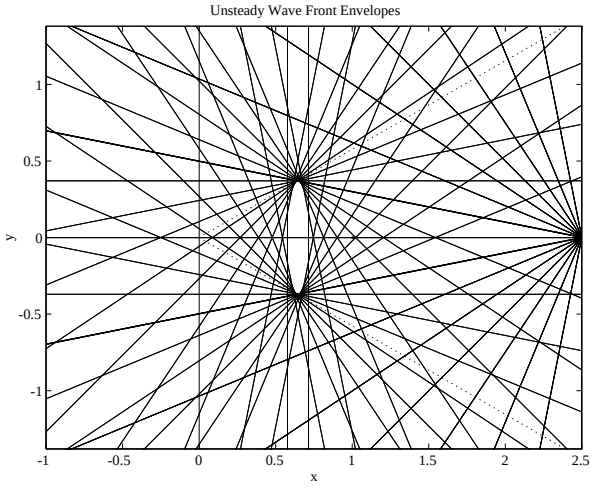

4f: Block-Jacobi Preconditioner.

Figure 4: 4th difference matrix dissipation.
Fourier footprint of high frequency modes and wave front envelopes.
$Re_{\Delta x} = \infty, M = 2.0, \frac{\Delta y}{\Delta x} = \frac{1}{5}, \frac{v}{u} = 0, \frac{\pi}{2} \leq \theta_x, \theta_y \leq \pi, \text{CFL} = 2.5.$

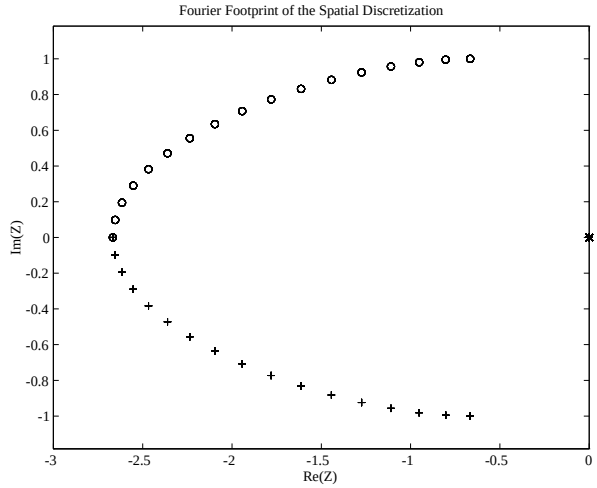

5a: Case 1.

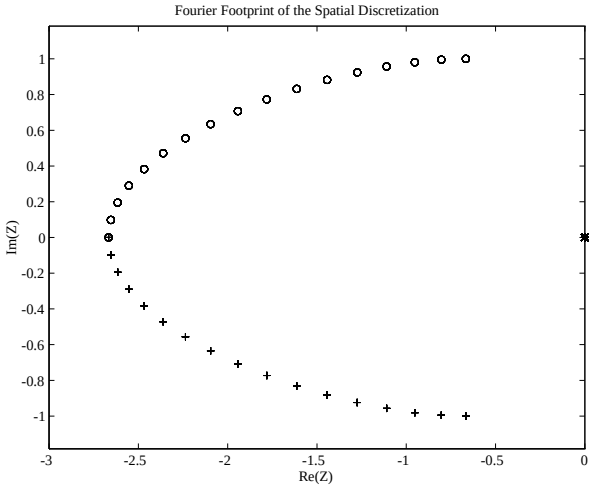

5b: Case 2.

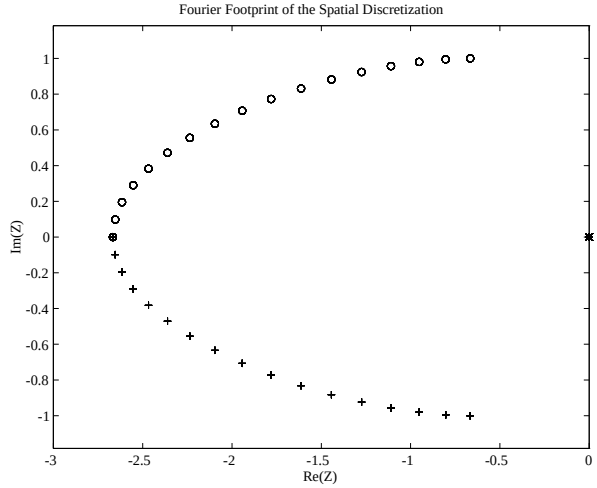

5c: Case 3.

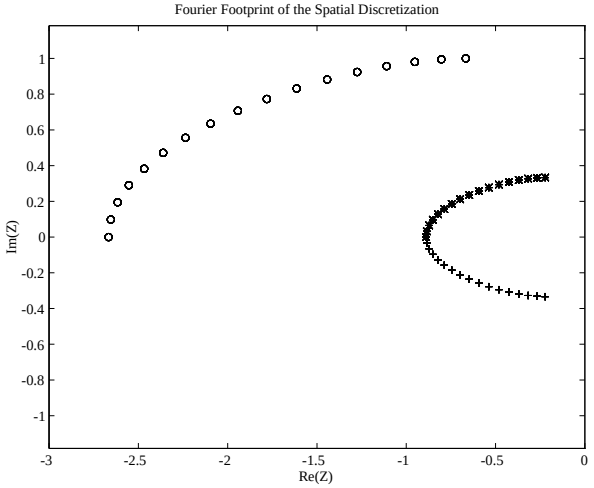

5d: Case 4.

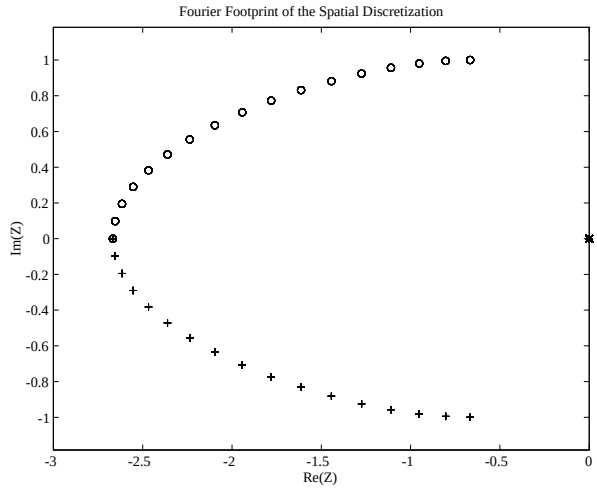

5e: Case 5.

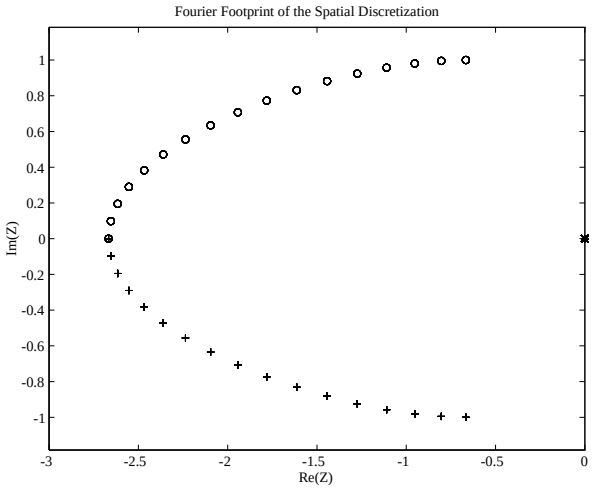

5f: Case 6.

Figure 5: Scalar Preconditioner.
Fourier footprint of high frequency modes in various asymptotic limits.
4th difference matrix dissipation. $\varepsilon^{(4)} = \frac{1}{6}, \pi/2 \leq \theta_x, \theta_y \leq \pi, \mathrm{CFL} = 1.0$.
See Tables 1,2,3 for Case, Analytic and Wave descriptions.

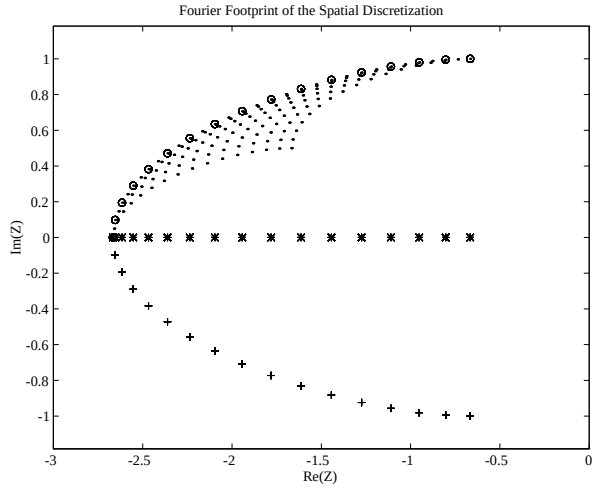

6a: Case 1.

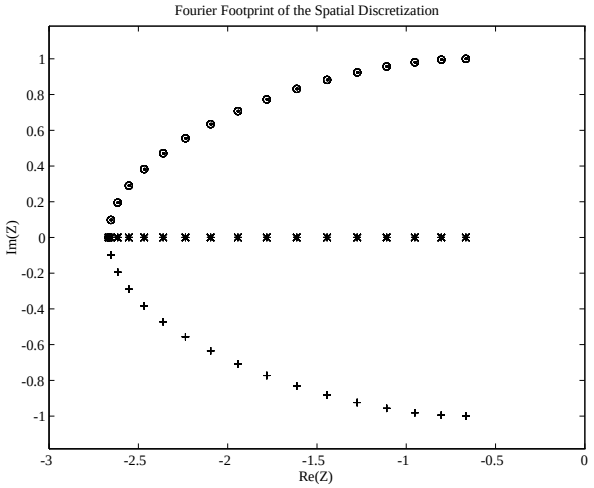

6b: Case 2.

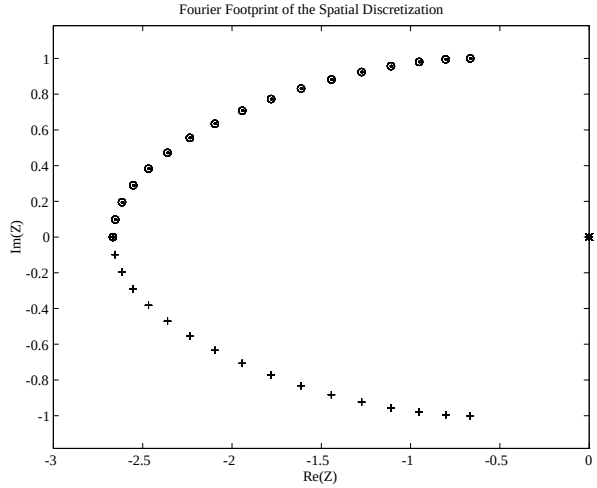

6c: Case 3.

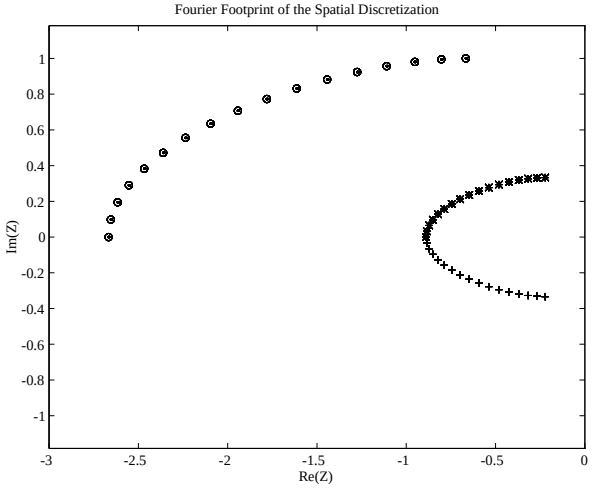

6d: Case 4.

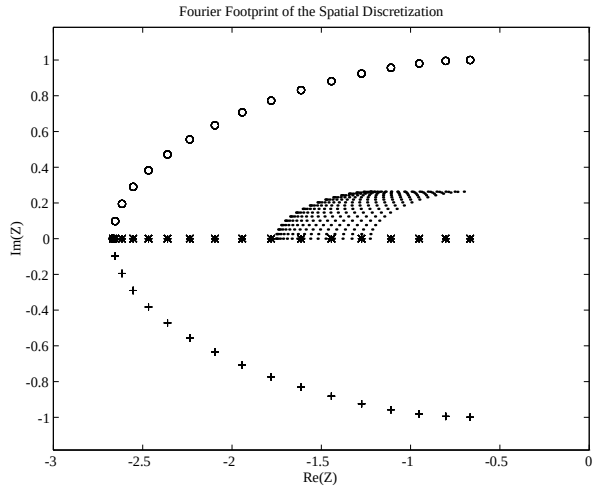

6e: Case 5.

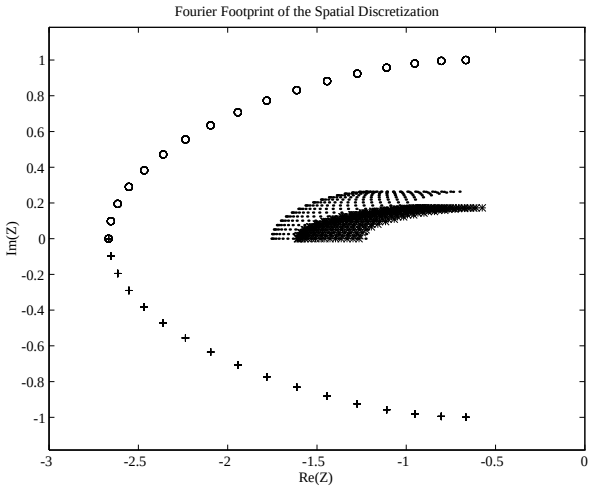

6f: Case 6.

Figure 6: Diagonal Preconditioner.
Fourier footprint of high frequency modes in various asymptotic limits.
4th difference matrix dissipation. $\varepsilon^{(4)} = \frac{1}{6}, \pi/2 \leq \theta_x, \theta_y \leq \pi, \mathrm{CFL} = 1.0$.
See Tables 1,2,3 for Case, Analytic and Wave descriptions.

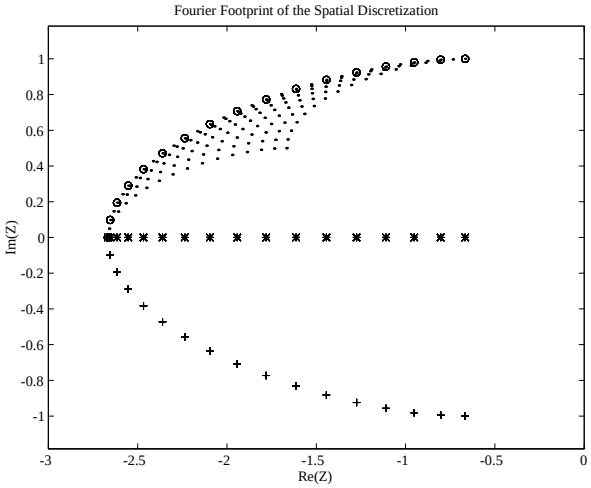

7a: Case 1.

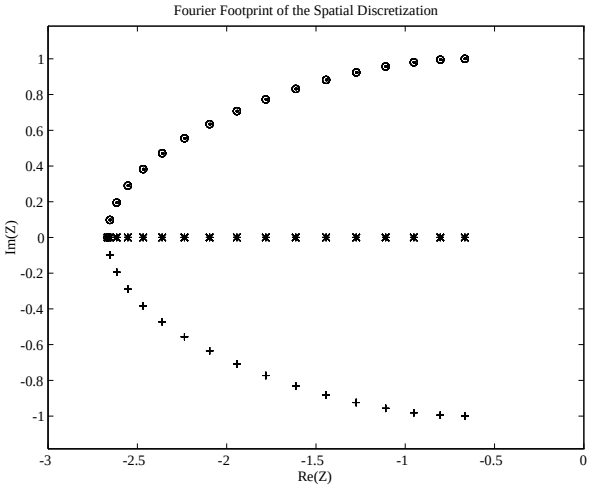

7b: Case 2.

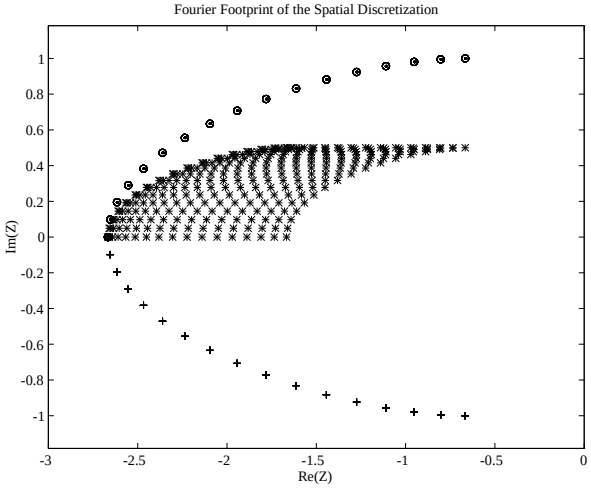

7c: Case 3.

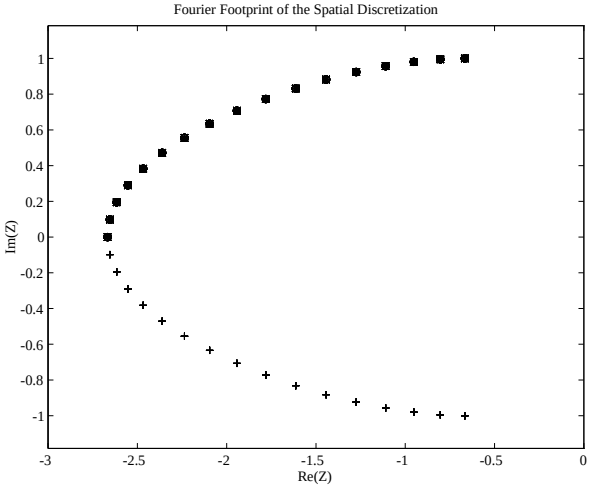

7d: Case 4.

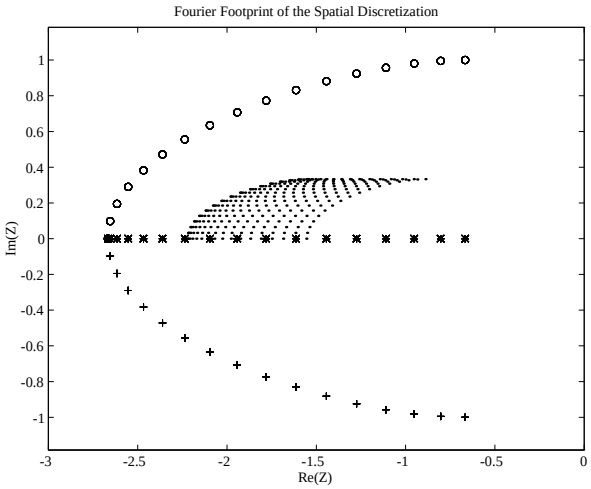

7e: Case 5.

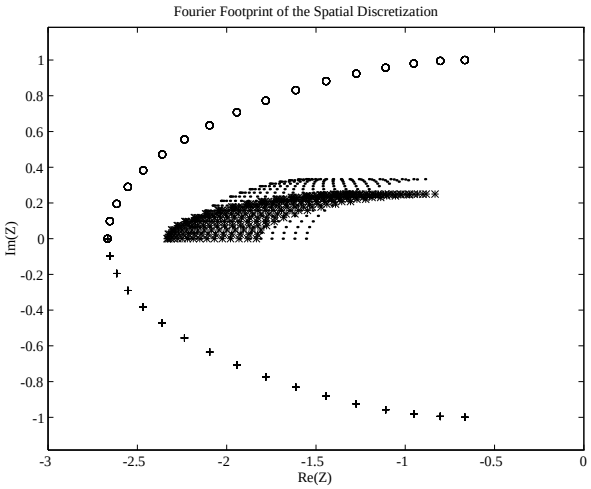

7f: Case 6.

Figure 7: Block-Jacobi Preconditioner.
Fourier footprint of high frequency modes in various asymptotic limits.
4th difference matrix dissipation. $\varepsilon^{(4)} = \frac{1}{6}, \pi/2 \leq \theta_x, \theta_y \leq \pi, \mathrm{CFL} = 1.0$.
See Tables 1,2,3 for Case, Analytic and Wave descriptions.

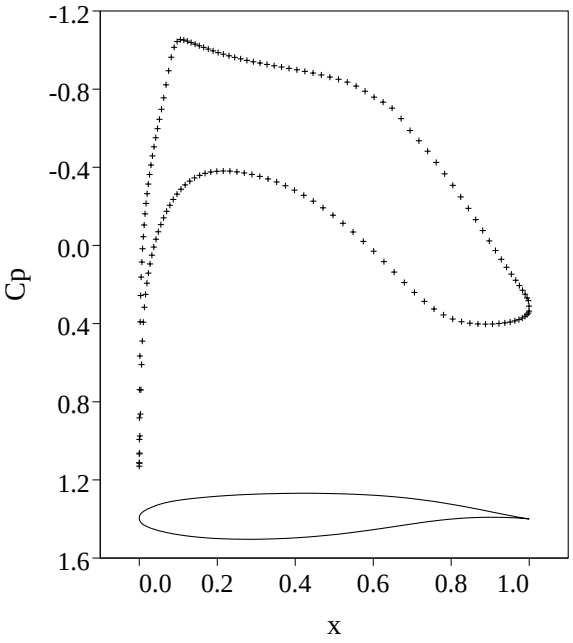

8a: C_p for Matrix Switch.
$C_l = .6252, C_d = .0002$

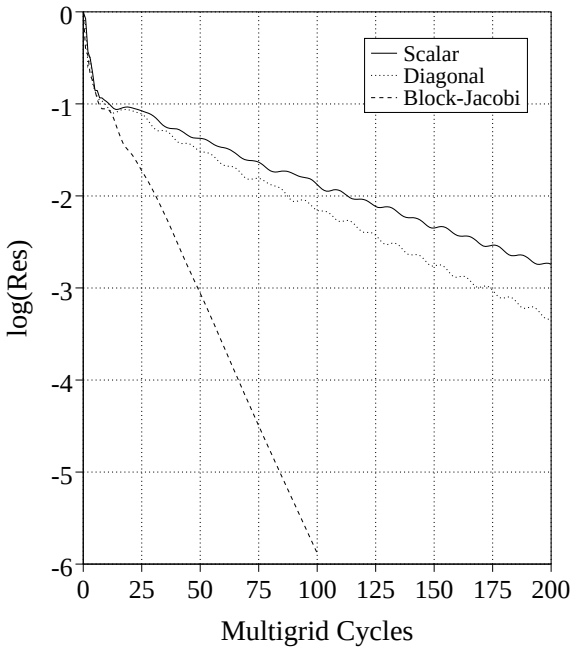

8b: Convergence for Matrix Switch.

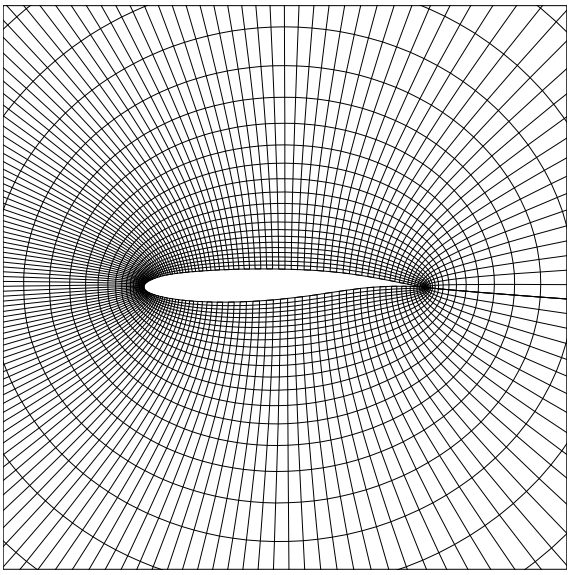

8c: Mesh.

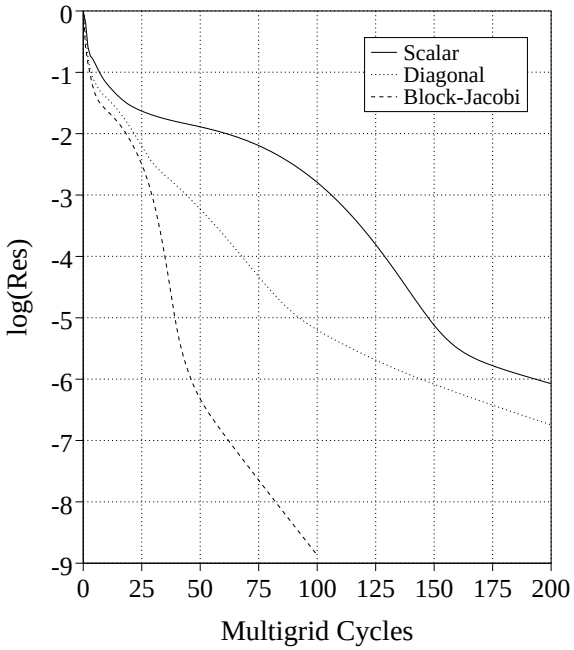

8d: Convergence for 1st Order Matrix Upwinding.

Figure 8: KORN Airfoil. $M_\infty = 0.75, \alpha = 0.0°$, 160×32 O-mesh. Matrix Switched Scheme.

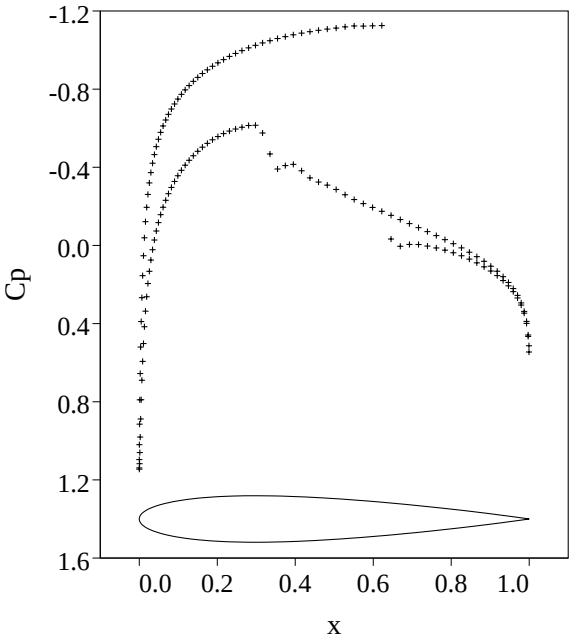

9a: C_p after 12 Multigrid Cycles.
$C_l = .3531, C_d = .0227$

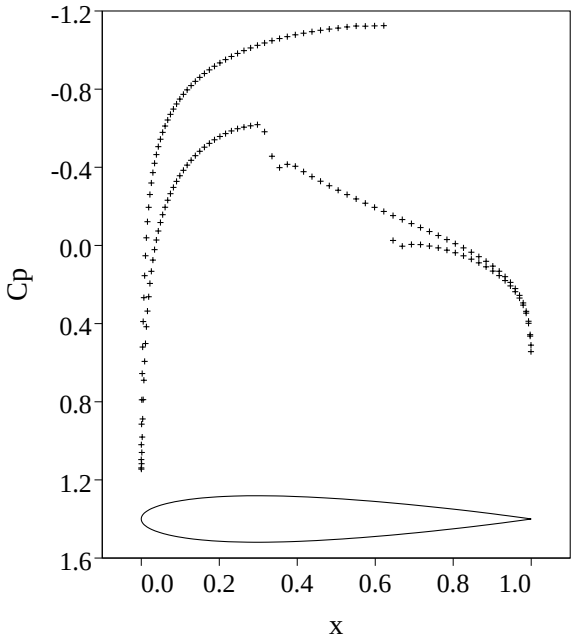

9b: C_p after 100 Multigrid Cycles.
$C_l = .3527, C_d = .0227$

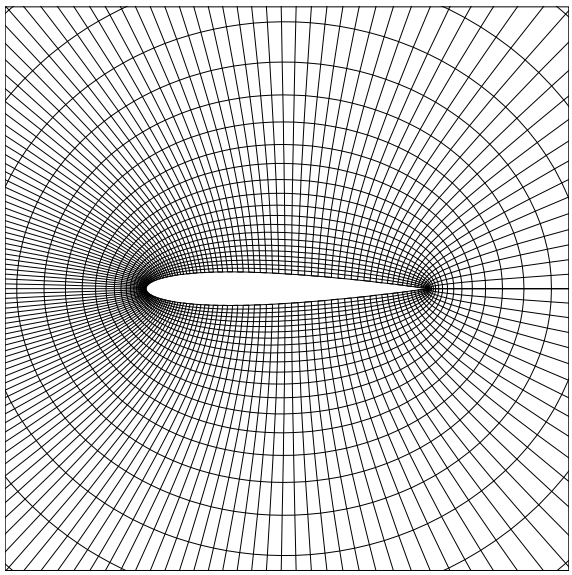

9c: Mesh.

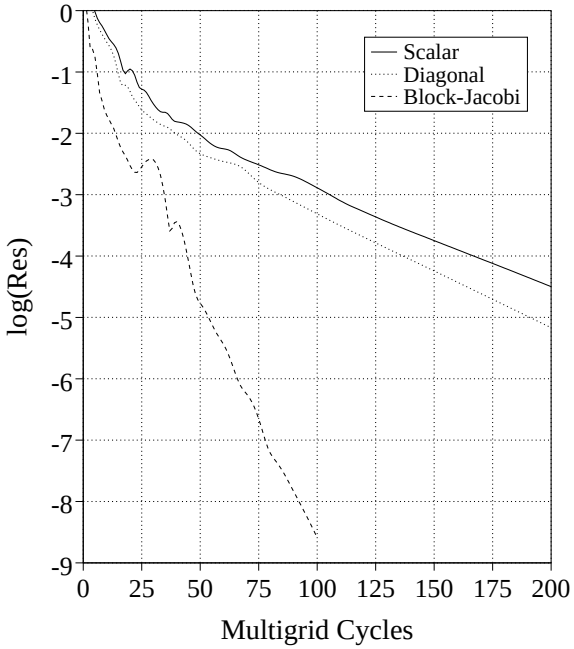

9d: Convergence.

Figure 9: NACA0012 Airfoil. $M_\infty = 0.8, \alpha = 1.25°$, 160×32 O-mesh.
Matrix Switched Scheme.

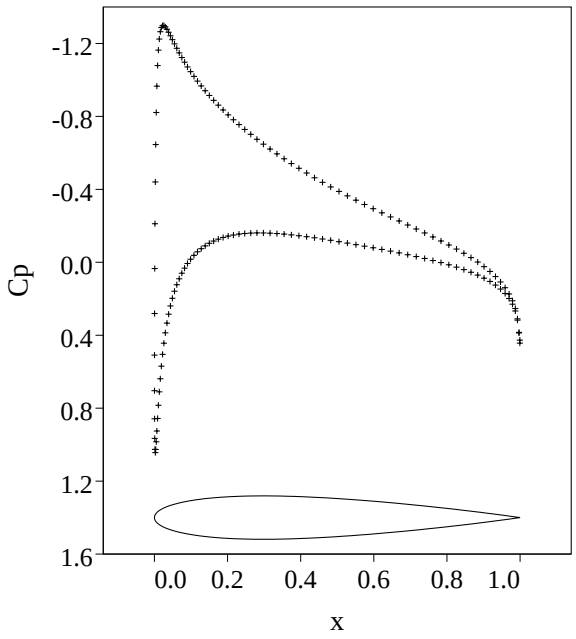

10a: C_p.
$C_l = .4260, C_d = .0001$.

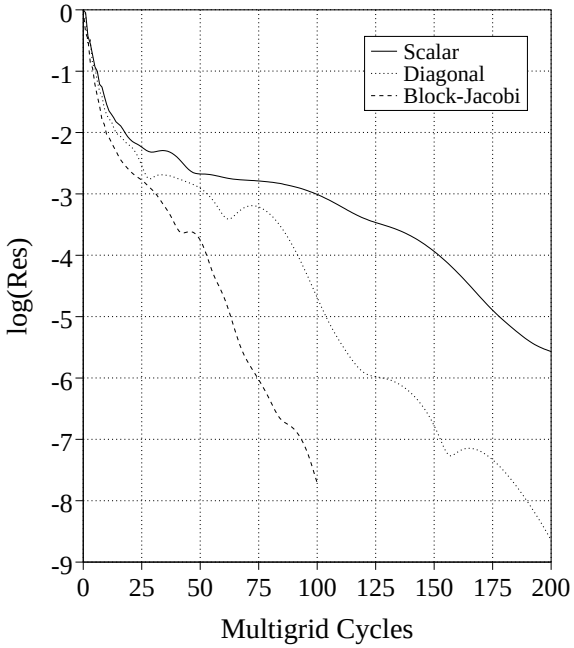

10b: Convergence.

Figure 10: NACA0012 Airfoil. $M_\infty = 0.5, \alpha = 3.0°$, 160×32 O-mesh.
Matrix Switched Scheme.

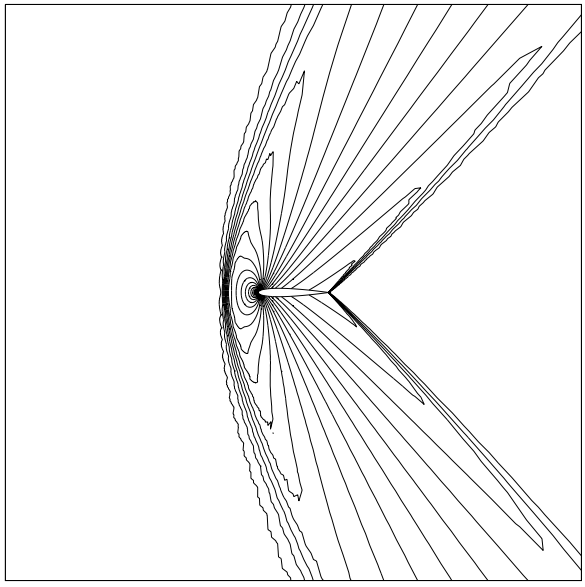

11a: Pressure Contours.
320×64 O-Mesh.

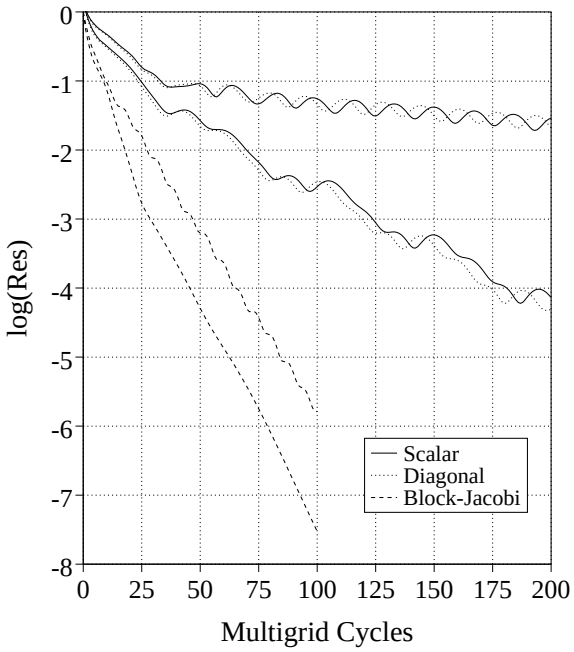

11b: Convergence Comparison.
160×32 and 320×64 O-Meshes.

Figure 11: NACA0012 Airfoil. $M_\infty = 1.2, \alpha = 0.0°$.
Matrix Switched Scheme.

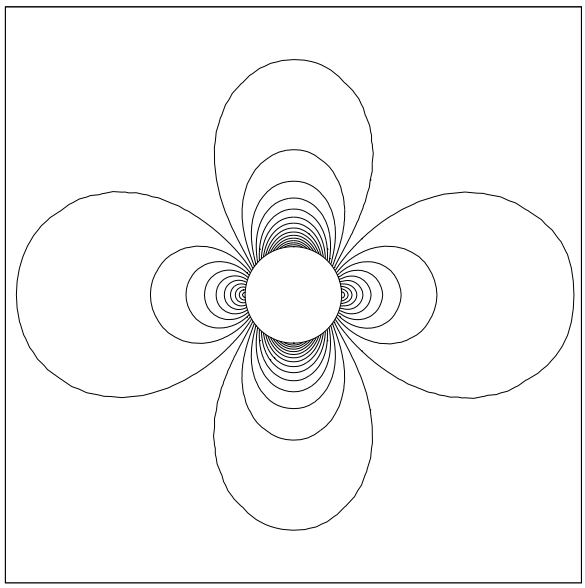

12a: Mach Number Contours.

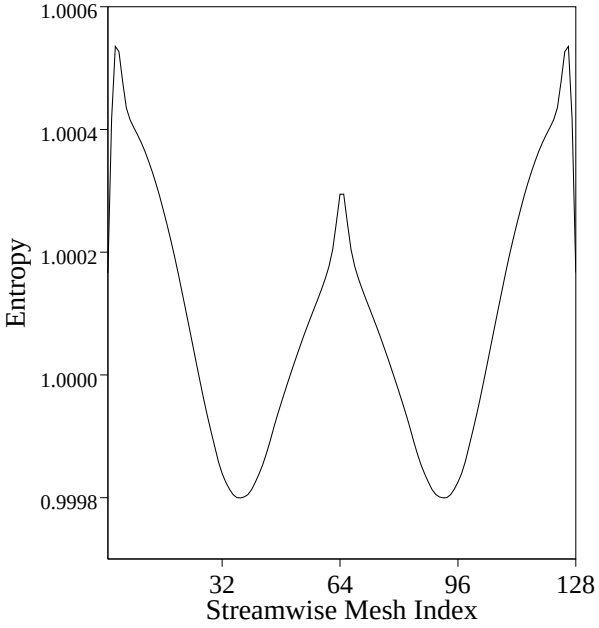

12b: Entropy Next to the Wall.
$s = \frac{p}{\rho^\gamma}$

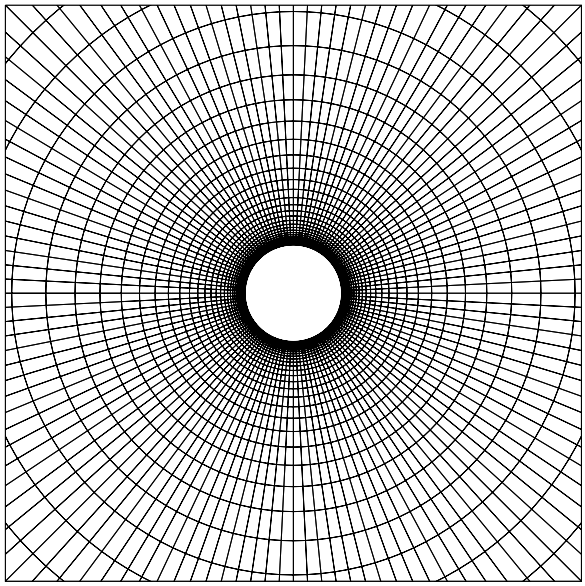

12c: Mesh.

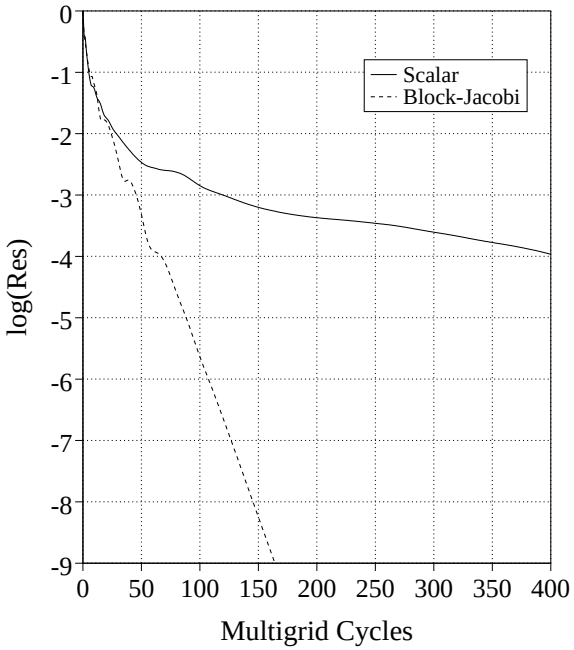

12d: Convergence.

Figure 12: Cylinder. $M_\infty = 0.38, \alpha = 0.0°$, 128×48 O-mesh.
Matrix Symmetric Limited Scheme.

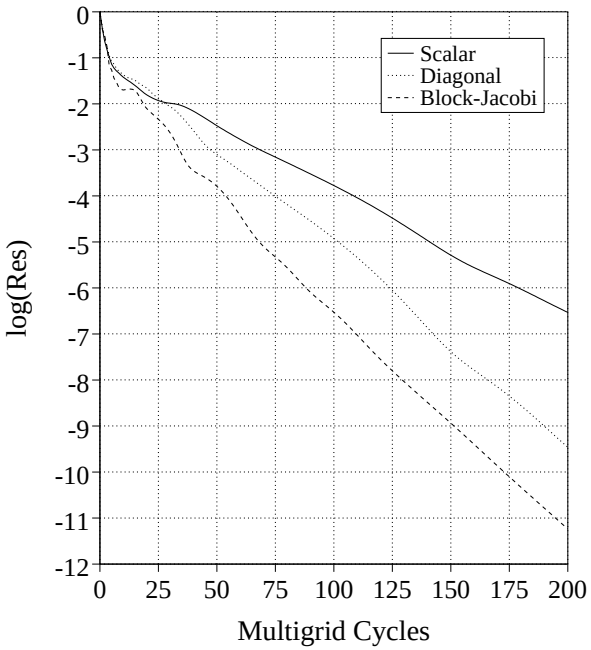

13a: Convergence.
Matrix Switched Scheme.

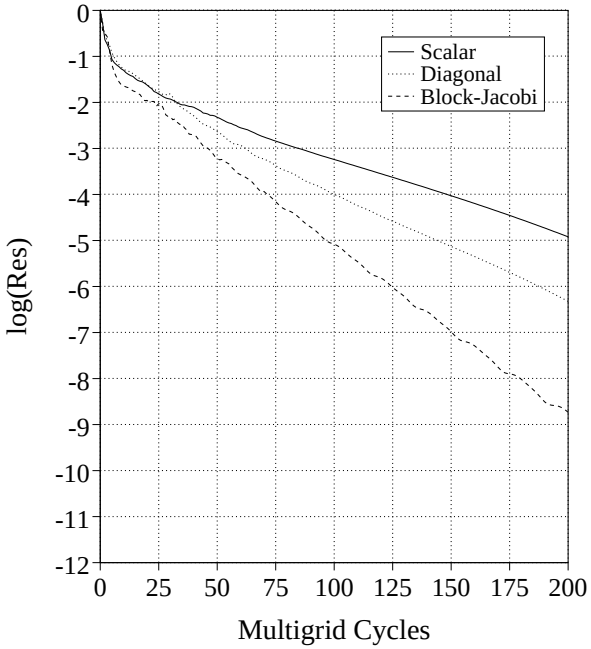

13b: Convergence.
Matrix Symmetric Limited Scheme.

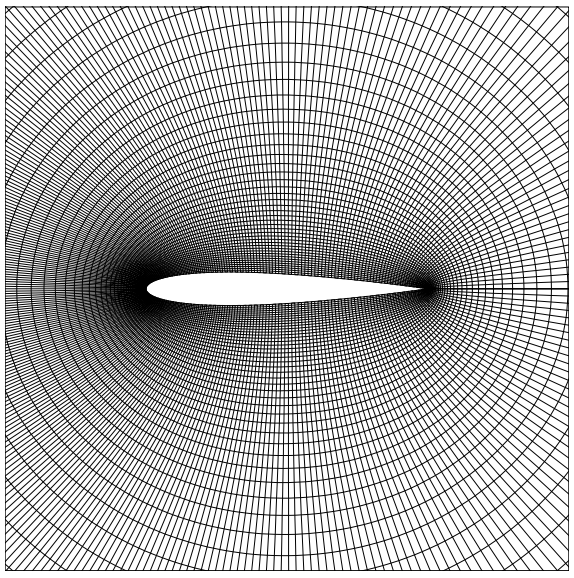

13c: Mesh.

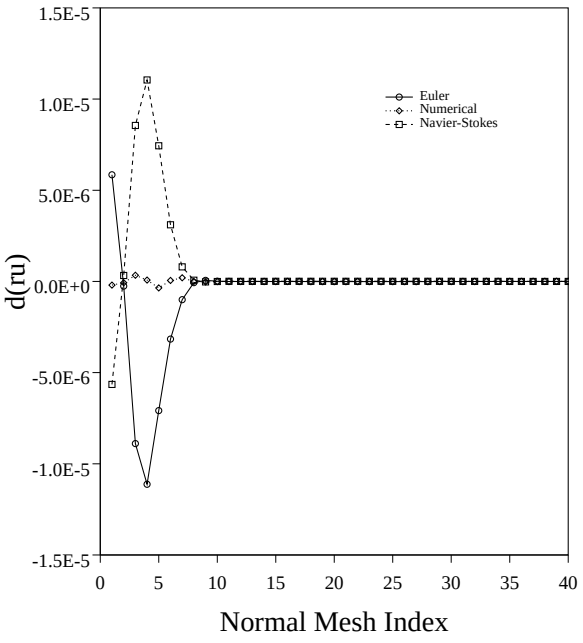

13d: Budget of X-Momentum Cell Updates for Matrix Switched Scheme.

Figure 13: NACA0012 Airfoil. $M_\infty = 0.5, \alpha = 0.0°, Re_L = 5{\times}10^3$, 320×64 O-mesh.

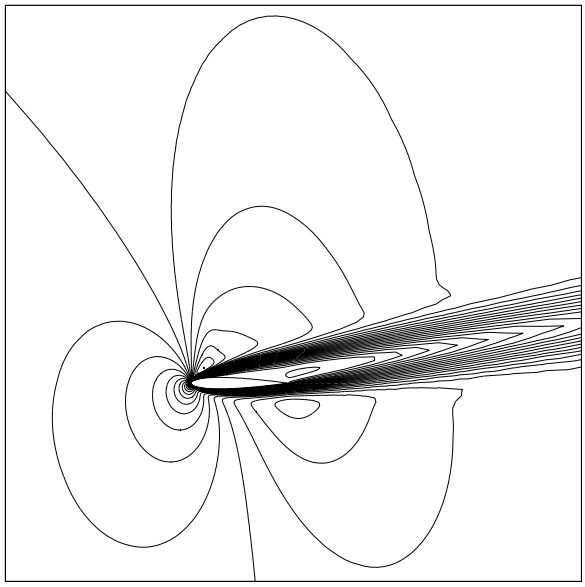

14a: Mach Number Contours.

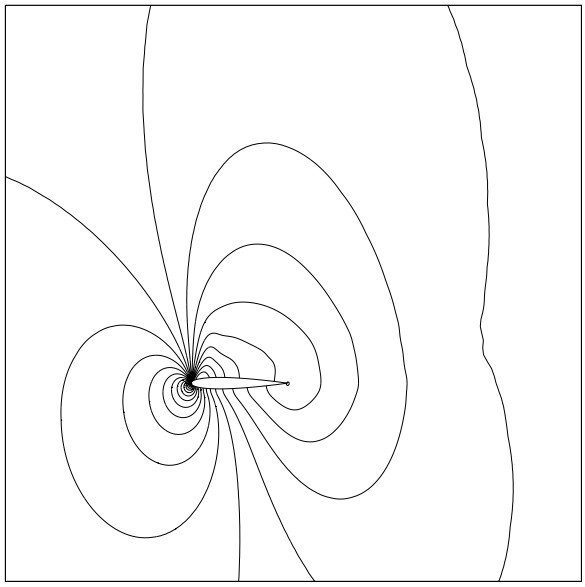

14b: Pressure Contours.

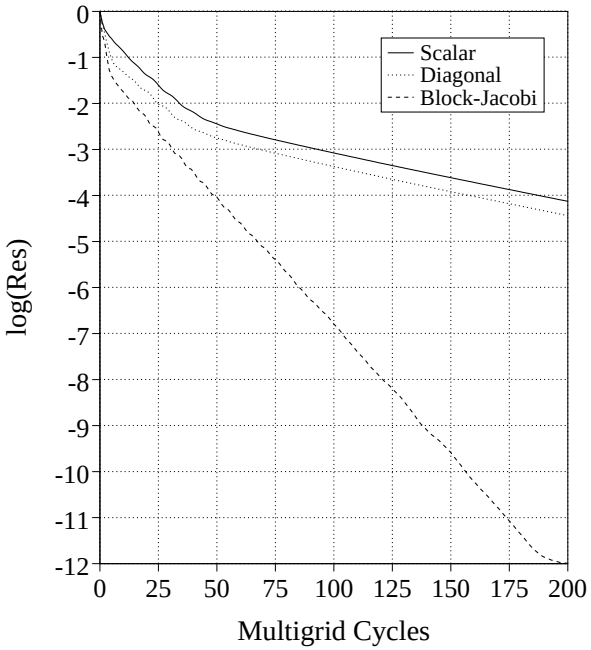

14c: Convergence.

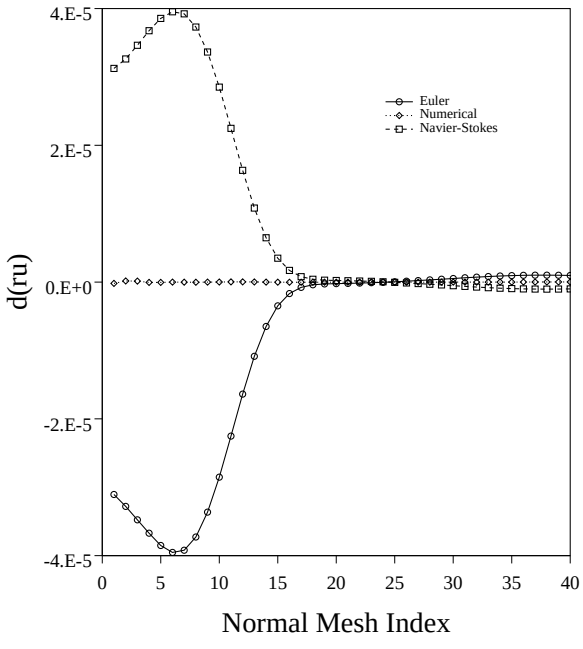

14d: Budget of X-Momentum Cell Updates.

Figure 14: NACA0012 Airfoil. $M_\infty = 0.8, \alpha = 10.0°, Re_L = 5{\times}10^2$, 320×64 O-mesh. Matrix Switched Scheme.

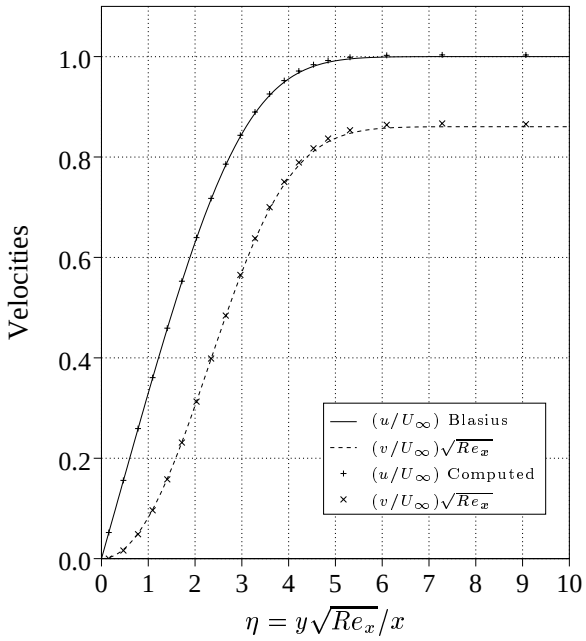

15a: Comparison to Blasius Velocity Profiles.

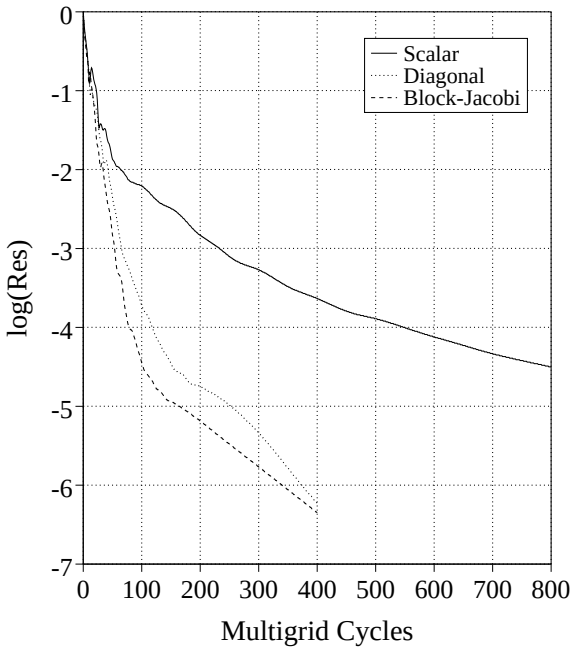

15b: Convergence.

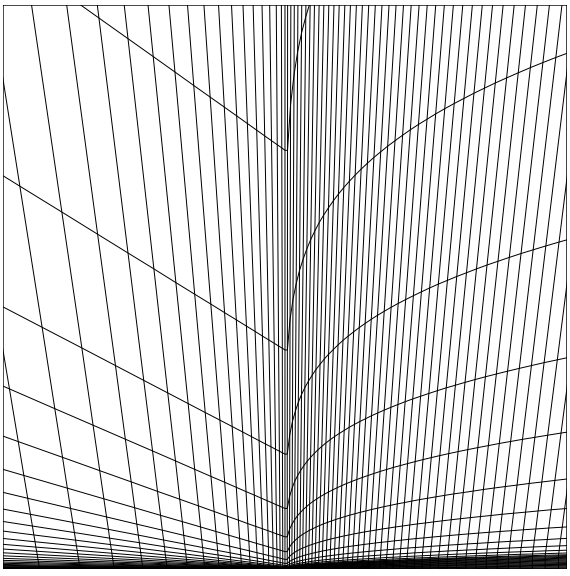

15c: Mesh at the Leading Edge. Magnification is 20% chord.

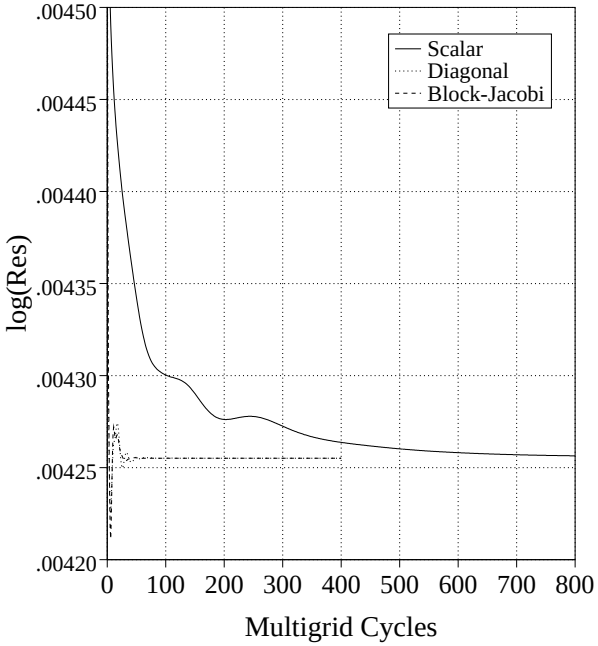

15d: C_D Convergence.

Figure 15: Flat Plate. $M_\infty = 0.15, \alpha = 0.0°, Re_L = 1{\times}10^5$, 128×32 H-mesh. Matrix Switched Scheme.

Acknowledgements

We wish to thank Prof. Antony Jameson for providing the mesh generator and Prof. Luigi Martinelli for assistance with many aspects of the code development.

References

[1] S. Allmaras, 1993. Analysis of a local matrix preconditioner for the 2-D Navier–Stokes equations. AIAA Paper 93-3330-CP, 11th Computational Fluid Dynamics Conference, Orlando, FL.

[2] S. Allmaras, 1995. Analysis of semi-implicit preconditioners for multigrid solution of the 2-D compressible Navier–Stokes equations. AIAA Paper 95-1651-CP, 12th Computational Fluid Dynamics Conference, San Diego, CA.

[3] A. Jameson, 1983. Solution of the Euler equations for two dimensional transonic flow by a multigrid method. MAE Report #1613, Princeton University.

[4] A. Jameson, 1983. Transonic flow calculations. MAE Report #1651, Princeton University.

[5] A. Jameson, 1984. A non-oscillatory shock capturing scheme using flux limited dissipation. MAE Report #1653, Princeton University.

[6] A. Jameson, 1992. Computational algorithms for aerodynamic analysis and design. MAE Report #1966, Princeton University.

[7] A. Jameson, 1993. Numerical wind tunnel – vision or reality. AIAA Paper 93-3021, AIAA 11th Computational Fluid Dynamics Conference, Orlando, Florida.

[8] A. Jameson, 1995. Analysis and design of numerical schemes for gas dynamics 1: Artificial diffusion, upwind biasing, limiters and their effect on accuracy and multigrid convergence. *Int. J. Comput. Fluid Dyn.*, **4**: 171–218.

[9] A. Jameson, 1995. Analysis and design of numerical schemes for gas dynamics 2: Artificial diffusion and discrete shock structure. *Int. J. Comput. Fluid Dyn.*, **5**: 1–38.

[10] A. Jameson, W. Schmidt and E. Turkel, 1981. Numerical solution of the Euler equations by finite volume methods using Runge-Kutta time stepping schemes. AIAA Paper 81-1259.

[11] W.-T. Lee, 1992. *Local Preconditioning of the Euler Equations.* PhD thesis, University of Michigan.

[12] L. Martinelli, 1987. *Calculations of Viscous Flows with a Multigrid Method.* PhD thesis, Princeton University.

[13] W.A. Mulder, 1989. A new multigrid approach to convection problems. *J. Comput. Phys.*, **83**: 303–323.

[14] W.A. Mulder, 1992. A high-resolution Euler solver based on multigrid, semi-coarsening and defect correction. *J. Comput. Phys.*, **100**: 91–104.

[15] N.A. Pierce, 1994. Characteristic-based dissipative schemes and characteristic time stepping for the Euler equations. Qualifying dissertation for DPhil status at Oxford University.

[16] P.L. Roe, 1981. Approximate Riemann solvers, parameter vectors, and difference schemes. *J. Comput. Phys.*, **43**: 357–372.

[17] S. Tatsumi, L. Martinelli and A. Jameson, 1994. Design, implementation, and validation of flux limited schemes for the solution of the compressible Navier-Stokes equations. AIAA Paper 94-0647, 32nd Aerospace Sciences Meeting and Exhibit, Reno, NV.

[18] S. Tatsumi, L. Martinelli and A. Jameson, 1995. A new high resolution scheme for compressible viscous flow with shocks. AIAA Paper 95-0466, 33rd Aerospace Sciences Meeting and Exhibit, Reno, NV.

[19] B. van Leer, 1989. Euler solvers for transonic applications. In *Transonic Symposium: Theory, Application and Experiment.* NASA.

[20] B. van Leer, W.-T. Lee and P.L. Roe, 1991. Characteristic time-stepping or local preconditioning of the Euler equations. AIAA Paper 91-1552-CP.